IOWA STATE UNIVERSITY
Digital Repository

2012

Electrical and capacitive methods for detecting degradation in wire insulation

Robert Thomas Sheldon
Iowa State University

Follow this and additional works at: https://lib.dr.iastate.edu/etd

Part of the <u>Electrical and Electronics Commons</u>, and the <u>Mechanics of Materials Commons</u>

Electrical and capacitive methods for detecting degradation in wire insulation

by

Robert T. Sheldon

A thesis submitted to the graduate faculty

in partial fulfillment of the requirements for the degree of

MASTER OF SCIENCE

Major: Electrical Engineering

Program of Study Committee:

Nicola Bowler, Major Professor

Brian K. Hornbuckle

Jiming Song

Iowa State University

Ames, Iowa

2012

To my parents, Kevin and Victoria, and my sister, Laura, for their neverending love and support.

TABLE OF CONTENTS

v

LIST OF TABLES

LIST OF FIGURES

ABSTRACT

Motivated by a need within the aerospace industry to detect and characterize degradation in the insulation of onboard wires, this thesis reports testing of several extant methods and development of novel capacitive sensors. This work focuses on measuring the electrical parameters resistance and capacitance that are directly related to the material parameters conductivity and permittivity, respectively, of the insulation. It is shown that the measured electrical parameters successfully indicate degradation in the wire insulation.

Insulation resistance tests were performed on 17 wire samples, removed from various locations on a retired aircraft, and compared with those conducted on pristine wire samples, in order to assess any change in conductivity exhibited by degraded insulation. Timed resistance tests were also performed to determine the dielectric absorption of the insulation. Curved patch-electrode sensors were applied in order to measure the capacitance and dissipation factor of the same wires. Results from the resistive and capacitive tests both identified wire samples that were apparently significantly degraded, as indicated qualitatively by visual inspection.

Further, a novel cylindrical interdigital capacitive sensor was developed. The interdigital sensor is designed with the goal of achieving a good signal-to-noise ratio, the lowest instrument error possible at 1 MHz, full circumferential coverage of the wire, and the ability to adjust the penetration depth of the electric field into the insulation layer by adjusting the separation of the sensor digits. With the aim, ultimately, of quantitative measurement of insulation complex permittivity, a numerical model was developed using a cylindrical Green's function and the Method of Moments to calculate theoretically the capacitance of the interdigital sensor. Benchmark experiments were carried out on large-scale dielectric-coated conductive cylinders to test the validity of the model. Experimental results agreed with measured results to within 5% for sensor configurations with 22 and 30 digits of each polarization, tested on insulation polymers acetal copolymer, acrylic and polytetrafluoroethylene. A design method by which

the penetration depth of the electric field into the insulation layer may be optimized is also introduced.

Plans for future work, to develop interdigital capacitive sensors with a convenient hand-held clamp design for in-situ testing of aircraft wiring insulation, are also presented.

CHAPTER 1.   GENERAL INTRODUCTION

1.1   Introduction

All insulated wires are subject to a variety of degradation modes, such as moisture, extreme temperatures, and mechanical stress. Failure of these wires in critical systems, such as aircraft and nuclear reactors, as a result of insulation degradation can be potentially hazardous and even fatal as these wires can transmit power, navigation and control signals. Although many wire testers and other nondestructive evaluation (NDE) techniques are commercially available, few are designed to actually characterize the insulation with the cylindrical geometry incorporated. It is purposed through the research presented in this thesis to develop a capacitive sensor to characterize wire insulation that builds from the foundation set by these extant techniques while incorporating the significant advantages of capacitive sensors developed previously for other applications. To achieve this, experiments were performed to measure and compare the resistance and capacitance of wire insulation, electrical parameters which are directly related to the material parameters conductivity and permittivity of the insulation, to determine the effectiveness of insulation characterization via the respective measurement techniques.

1.2   Literature survey

1.2.1   Extant methods of insulation characterization

A wire is essentially comprised of two components - a conductor and an insulator - which means that there are two types of problems, or faults, that may eventually occur in a wire over time. A common method of detecting conductor faults, or "hard faults", is known as time-domain reflectometry (TDR), whereby a voltage pulse is transmitted along the central conductor of the wire and the reflection pulse return time and magnitude are used to determine

the location and impedance type of the discontinuity [1]. For insulation faults, known as "soft faults", a similar form of testing is used and is known as partial discharge (PD) analysis, which is used to detect and locate regions of insulation that are at risk of suffering electrical arcing damage. PD analysis works by applying a high voltage pulse on the conductor, which partially discharges its energy in degraded regions, the occurrence of which partially reflects the incident pulse and can be used to locate and characterize the soft faults [1].

Another common soft fault detector is an insulation resistance (or leakage current) tester that simply works by applying a high direct-current voltage to the conductor and measuring the leakage current through the insulation at various points along the wire. Factors such as mechanical damage, vibration, extreme temperatures, dirt, oil, corrosive vapors, and humidity are all known to decrease the resistance of various insulating media causing them to become more conductive [2]. All of these techniques suffer from the significant disadvantage of requiring access to the central conductor, which may not be possible, and applying to it a high voltage, which may be dangerous and may promote further degradation to the insulation under test.

1.2.2 Capacitive sensing

Capacitive sensing is ideally suited for characterizing dielectric materials due to the linear relationship between the measured capacitance and the relative permittivity (dielectric constant) of the material, the lack of need to access the central conductor of the wire, and independence of the measured capacitance on the applied voltage. A basic parallel-plate capacitor is shown in Figure 1.1(a) where the electric field lines are completely parallel to each other and perpendicular to two parallel plate electrodes [3]. As the parallel plates are manipulated onto the same plane in Figure 1.1, the electric field fringes outward into the dielectric medium of interest. In [4] a simple coplanar electrode pair, shown in Figure 1.2, is examined in which an alternating, yet quasistatic, excitation potential is placed on a source electrode and the current through the receiver electrode is measured. The phase difference and magnitude of the potential and current determine the complex impedance, the reactive component of which yields the measured capacitance provided that the operating frequency is known. An important observation is made in [5] that a sinusoidal variation of the electric field in the plane of the
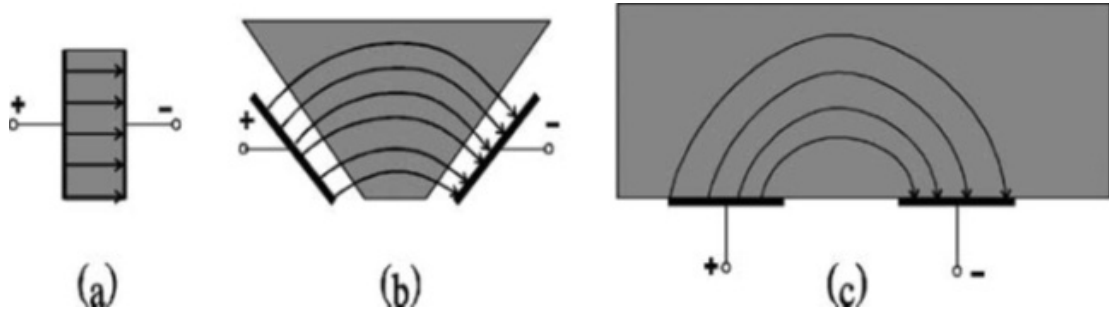
Figure 1.1 Progressive transformation of (a) a basic parallel plate capacitor into (c) a coplanar capacitive sensor [3].
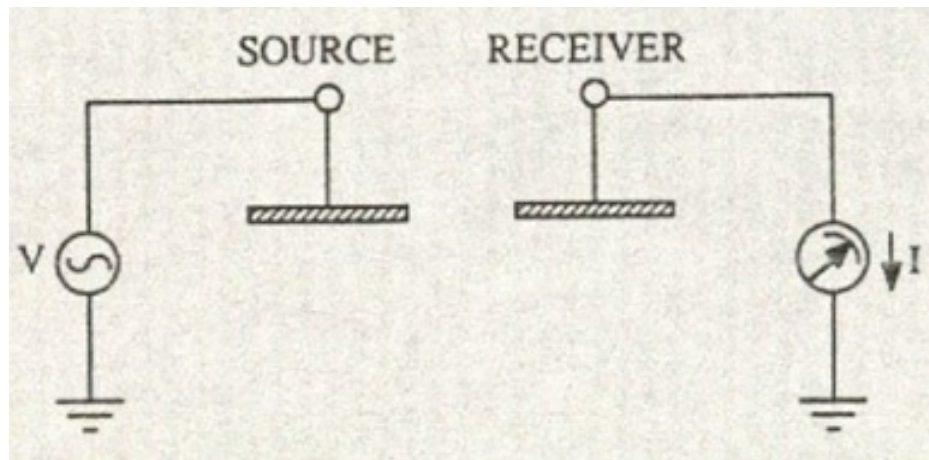
Figure 1.2 A circuit schematic of a basic capacitance measurement of two coplanar electrodes whereby an alternating electric potential V on the source electrode excites a current I through the receiver electrode [4]. The calculated complex impedance and operating frequency then determine the capacitance.

electrodes must be accompanied by an exponentially-decaying field in the direction orthogonal to the plane, according to the particular solution to the Laplace equation.

An analytical formula is given in [6] to solve for the capacitance as a function of the width and separation of the two electrodes and the thickness and permittivity of two finite dielectric layers. In this case, shown in Figure 1.3, the theoretical model is comprised of two perfectly conducting electrodes of infinitesimal thickness, width s, spacing $2g$, dielectric layers of heights h_1 and h_2 from the electrode surface, and relative permittivity values of ϵ_{r1} and ϵ_{r2}, respectively. The solution per unit length is given by [6] as

$$C = \epsilon_0 \epsilon_{\text{eff}} \frac{K(k_0')}{K(k_0)}, \tag{1.1}$$

4

where ϵ_0 is the permittivity of free space and $K(k)$ is the complete elliptic integral of the first kind, given by

$$K(k) = \int_0^{\pi/2} \frac{1}{\sqrt{1 - k^2 \sin^2 \theta}} d\theta, \tag{1.2}$$

k is the modulus of the integral, given by

$$k_0 = \frac{g}{s + g} \tag{1.3}$$

$$k_0' = \sqrt{1 - k_0^2}, \tag{1.4}$$

and ϵ_{eff} is the effective permittivity beneath the surface of the electrodes, given by

$$\epsilon_{\text{eff}} = 1 + (\epsilon_{r1} - 1)q_1 + (\epsilon_{r2} - \epsilon_{r1})q_2, \tag{1.5}$$

where

$$q_i = \frac{1}{2} \frac{K(k_i')K(k_0)}{K(k_i)K(k_0')}, \qquad i = 1, 2 \tag{1.6}$$

$$k_i = \frac{\tanh\left(\frac{\pi g}{2h_i}\right)}{\tanh\left(\frac{\pi(s+g)}{2h_i}\right)}, \qquad i = 1, 2 \tag{1.7}$$

and

$$k_i' = \sqrt{1 - k_i^2}, \qquad i = 1, 2. \tag{1.8}$$

This simple two-element structure can also be modeled as two capacitors in parallel, with one being the capacitance between the electrodes surrounded by free space and the other being a half-space of permittivity $\epsilon_{r1} - 1$ [7].

The simple coplanar electrode pair can be expanded to an array, most often called interdigital electrodes, whereby many parallel electrode fingers, or digits, are coplanar with one another. This structure, shown in Figure 1.4, has the advantage being less susceptible to external noise while also greatly increasing the capacitance. In [8] the interdigital array is modeled by a series of capacitors that represent the half capacitance between a particular electrode and the zero-potential plane between two neighboring oppositely-charged electrodes. From this basic model, an analytical formula was developed that is a function of the spatial periodicity of the electrodes and the total electrode metallization ratio as well as the thickness and permittivity
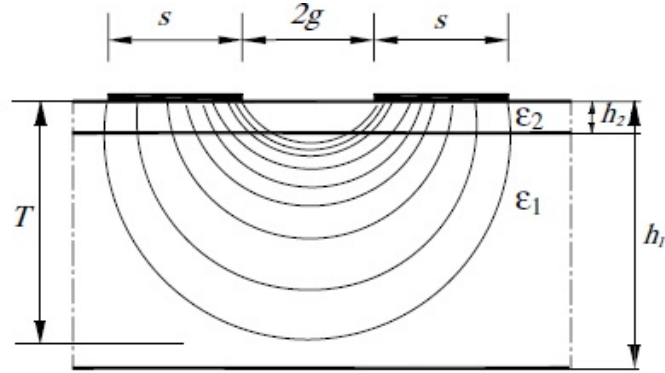
Figure 1.3   A coplanar capacitive sensor modeled over two dielectric layers of finite thickness h_1 and h_2 and permittivity values ϵ_1 and ϵ_2, respectively. The two infinitesimally-thin electrodes each have a width s and are separated by a distance of $2g$ [6].
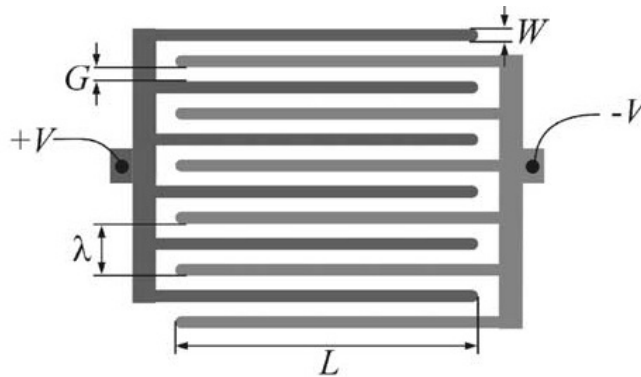
Figure 1.4   Layout of a planar interdigital capacitive sensor, comprised of two electrodes of opposing polarities, $+V$ and $-V$, with a number of interlocking "digits" of width W, spacing G, length L, and spatial periodicity λ [8].

of the interrogated layers. Interdigital array performance and potential applications are investigated in [3]. Capacitive sensors in general are particularly useful as moisture and rain sensors [9] and as embedded or external monitors of the polymeric curing process [10].

For test-pieces that are of cylindrical geometry, a numerical calculation method was developed in [11] that utilizes cylindrical Green's functions and the Method of Moments to solve for the electrode charge distribution and, hence, the total capacitance. The electrodes themselves consist of two curved patch-electrodes that conform to the surface of an infinitely-long dielectric rod. A perfectly-conducting central conductor core is added to the dielectric rod in [12] to create a geometry that most closely resembles that of a real wire. Empirical and analytical

formulae are developed for determining the capacitance of a planar interdigital array that is used in [13] to detect damage in power system cable insulation.

Wire insulation degradation is also shown in [12] to be detected as a measurable change in the electrical permittivity of the insulation. Real insulation has, in fact, a complex permittivity, defined as $\epsilon^* = \epsilon' - j\epsilon''$, arising from the fact that real insulation is not a perfect insulator. The real (ϵ') and imaginary (ϵ'') components of complex permittivity are derived from Maxwell's law of total currents, which is given in the following time-harmonic form and assuming no frequency-dependent relaxations:

$$\mathbf{J}_t = \mathbf{J}_c + \mathbf{J}_d = \sigma\mathbf{E} + j\omega\epsilon'\mathbf{E} = j\omega\epsilon_0\left(\epsilon_r - j\frac{\sigma}{\omega\epsilon_0}\right)\mathbf{E}, \tag{1.9}$$

where $\mathbf{J}_t$ is the total current density, $\mathbf{J}_c$ is the conduction current density, $\mathbf{J}_d$ is the displacement current density, $j = \sqrt{-1}$, σ is the conductivity, and ω is the angular frequency. From this law, the real component of permittivity is thus defined as $\epsilon' = \epsilon_r\epsilon_0$, where ϵ_r is the relative permittivity of the material and ϵ_0 is the permittivity of free space, while the imaginary component is defined as $\epsilon'' = \sigma/\omega$. By subjecting wire insulation to periods of extremely high temperatures, such as may occur onboard an aircraft, it is shown in Figures 1.5(a) and 1.5(b) that both components of the complex permittivity exhibit an increase with increasing exposure time and temperature. Permittivity changes also occur due to exposure to various types of fluids and due to mechanical stress, both of which are likely conditions on board an aircraft [14]. It is, therefore, the goal of the research presented in this thesis, and of future work, to design a sensor capable of detecting such changes in the permittivity in the form of a measurable changes in the sensor capacitance and dissipation factor (discussed in Chapter 3).

1.3   Thesis structure

The research presented in this thesis is divided among three core chapters that are intended to show a progressive approach toward the final design of a new sensor that can detect undesirable changes in the insulation of wires. In Chapter 2, theoretical investigations of a long, dielectric-coated conductive circular cylinder embedded in a static and uniform electric field oriented perpendicular to the cylinder axis are conducted to determine the response of that

(a) Real part
(b) Imaginary part
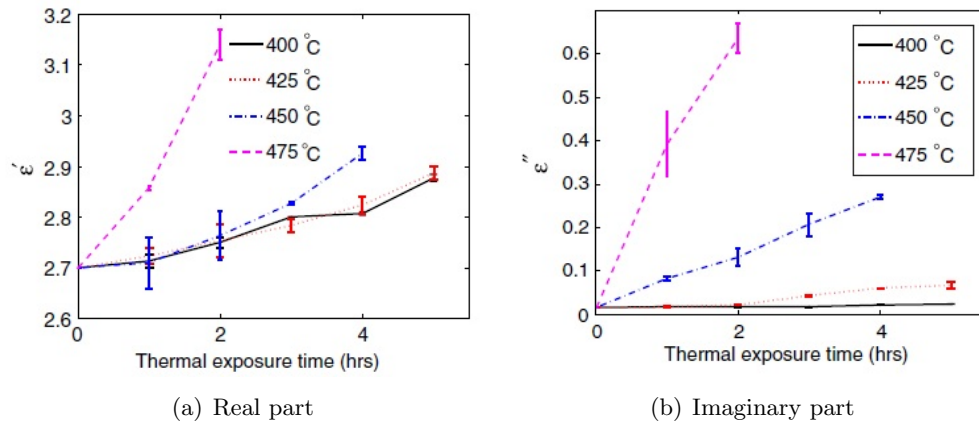
Figure 1.5   Inferred complex insulation permittivity of thermally exposed MIL-W-81381/12 wires. Error bars denote standard deviation of six measurements [12].

field to the presence of the cylinder. This electric field is a simplified analytical model that represents the cylindrical geometry and symmetrical nature of two sources of opposite polarity placed on opposite sides of a wire, much like two electrodes placed in the same locations. The effect of a varying central conductor electric potential on the electric field, and the capacitance of a system in which identical series capacitors are separated by a varying potential are also investigated.

Extant methods of wire insulation characterization are employed experimentally in Chapter 3. The most widely and currently used method is resistance testing, measured with an instrument known simply as an insulation tester, and was tested on 17 wire samples removed from a retired aircraft for the purpose of determining ionic and dipole absorption indicators of degradation within the insulation. On these same wires, insulation capacitance and dissipation factor was measured utilizing a curved patch-electrode capacitive sensor.

Finally, Chapter 4 discusses a new cylindrical interdigital capacitive sensor that was designed to achieve a higher signal-to-noise ratio and greater circumferential coverage of the wire insulation than the curved patch-electrodes. For this new electrode configuration, the electro-quasistatic theory is developed, benchmark experiments were performed, and the penetration depth of the electric field into the insulation optimized.

1.4   References

[1] C. Desai, K. Brown, M. Desmulliez and A. Sutherland, "Selection of Wavelet for De-noising PD waveforms for Prognostics and Diagnostics of Aircraft Wiring", *Annual Report Conference on Electrical Insulation and Dielectric Phenomena*, pp. 17-20, 2008.

[2] *A Stitch in Time: The Complete Guide to Electrical Insulation Testing*. Dallas: Megger, 2006.

[3] A. V. Mamishev, K. Sundara-Rajan, F. Yang, Y. Du, and M. Zahn, " Interdigital sensors and transducers", *Proc. IEEE*, Vol. 92, pp. 808-845, 2004.

[4] M. Gimple and B. A. Auld, "Position and Sample Feature Sensing with Capacitive Array Probes", *Review of Progress in QNDE*, edited by D. O. Thompson and D. E. Chimenti, pp. 509-513, 1987.

[5] B. A. Auld, J. Kenney and T. Lookabaugh, "Electromagnetic sensor arrays - theoretical studies", *Review of Progress in QNDE*, edited by D. O. Thompson and D. E. Chimenti, pp. 681-690, 1985.

[6] A. A. Nassr, W. H. Ahmed, and W. W. El-Dakhakhni, " Coplanar capacitance sensors for detecting water intrusion in composite structures", *Meas. Sci. Technol.*, Vol. 19, pp. 075702(7pp), 2008.

[7] A. A. Nassr and W. W. El-Dakhakhni, "Non-destructive evaluation of laminated composite plates using dielectrometry sensors", *Smart Mater. Struct.*, Vol. 18, 2009.

[8] R. Igreja and C. J. Dias, "Analytical evaluation of the interdigital electrodes capacitance for a multi-layered structure", *Sensor Actuat. A-Phys.*, Vol. 12, pp. 291-301, 2004.

[9] I. Bord, P. Tardy and F. Menil, "Influence of the electrodes configuration on a differential capacitive rain sensor performances", *Sensors and Actuators B: Chemical*, Vol. 114, No. 2, pp. 640-645, 2006.

[10] D. R. Day, "Microdielectric sensors for cure control and materials evaluation", *Review of Progress in QNDE*, pp. 1037-1046, 1985.

[11] T. Chen, N. Bowler and J. R. Bowler, "Analysis of Arc-Electrode Capacitive Sensors for Characterization of Dielectric Cylindrical Rods", *IEEE Trans. Instr. Meas.*, Vol. 61, No. 1, pp. 233-240, 2012.

[12] T. Chen and N. Bowler, "Analysis of a capacitve sensor for the evaluation of circular cylinders with a conductive core", *Meas. Sci. Technol.*, Vol. 23, 045102(10pp), 2012.

[13] R. H. Bhuiyan, R. A. Dougal and M. Ali, "Proximity Coupled Interdigitated Sensors to Detect Insulation Damage in Power System Cables", *IEEE Sensors Journal*, Vol. 7, No. 12, pp. 1589-1596, 2007.

[14] L. Li, "Dielectric properties of aged polymers and nanocomposites", *Theses and Dissertations*, Paper 12128, Iowa State University, 2011.

CHAPTER 2.   ELECTRIC FIELDS AND CAPACITIVE EFFECTS OF A CHARGED DIELECTRIC-COATED CONDUCTIVE CYLINDER

2.1   Introduction

In the field of nondestructive evaluation (NDE), recent developments have advanced the usage of capacitive sensors for insulating or dielectric materials. These sensors use electrodes, placed on the test piece, to measure the sensor capacitance in the area of interest. Degradation or damage to the insulating test piece will change the local relative permittivity of the material, allowing the change to be measured as a change in sensor capacitance. For example, two electrodes placed across an insulated wire will result in a measured value of capacitance that depends upon the the permittivity of the insulation, the diameters of the central conductor and the surrounding insulation, and the geometry of the electrodes [1].

During the course of this research, a question was raised as to how an electric potential on the central conductor of the wire-under-test would affect capacitance measurements. This situation could arise when testing wires onboard an airplane that cannot be de-energized for a variety of reasons. A mathematical analysis was performed to investigate this concern and any possible measurement ramifications. From the electric field analysis conducted in the following section, it was determined that a charged conductor indeed creates an imbalance of charges on the electrodes, but whether the total capacitance is affected was the main question.

Although the capacitance of the test piece can be used to detect a flaw or location of degradation, it would also be of interest to plot the response of the locally-generated electric field due to the presence of the flaw or degradation. It is, therefore, informative to consider the case of dielectric-coated conductive cylinder embedded in a static and uniform electric field that represents the field generated by two remotely-located source electrodes on opposing sides
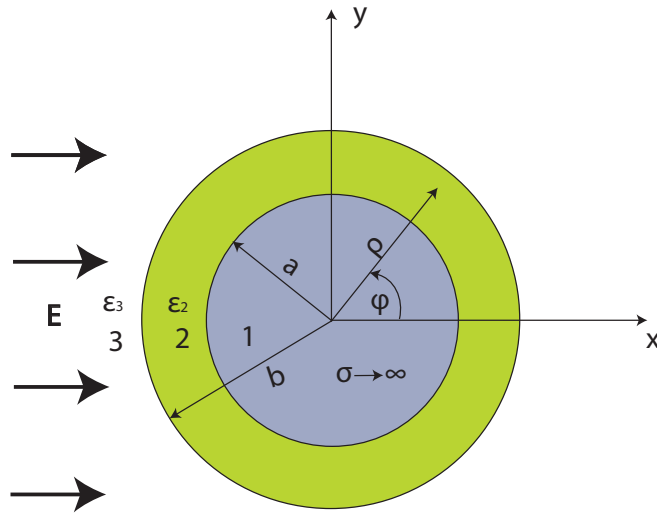
Figure 2.1   Cross-section of dielectric-coated conductive cylinder placed in a uniform electric field **E**.

of the cylinder. This conductor may be energized, such as in a real-world case, and thus the electric potential of which must be considered. Because there are two sources generating two different electric fields in this example - the external electric field and the conductor - the following derivations deal with each source separately and are then superimposed to generate the final field. Effects on the capacitance of a generic symmetric capacitive sensor from this central source is also discussed in a thought experiment.

2.2   Dielectric-coated, uncharged cylindrical conductor in a uniform electric field

2.2.1   Polar solution to the Laplace equation

Consider a cylinder, with its axis along the z-axis, comprised of a perfect electrical conductor ($\sigma \to \infty$) of radius a held at zero potential and a surrounding dielectric layer of relative permittivity ϵ_2 and radius b, placed in a dielectric medium of permittivity ϵ_3 in which exists a uniform electric field defined as $\mathbf{E} = E_0 \hat{x}$. This field is theoretically generated by infinitely-large parallel plate electrodes that are spaced apart at a finite distance. The introduction of this cylinder, a cross-section of which is shown in Figure 2.1, to the infinite region disturbs the

original electric field and leads to three different regional electric fields. These fields can be found using the relationship between the electric field and electrostatic potential Ψ, expressed as

$$\mathbf{E} = -\nabla\Psi. \tag{2.1}$$

Ψ is found by solving Laplace's Equation expressed by

$$\nabla^2\Psi = 0, \tag{2.2}$$

which, in polar coordinates, is written as

$$\frac{1}{\rho}\frac{\partial}{\partial\rho}\left(\rho\frac{\partial\Psi}{\partial\rho}\right) + \frac{1}{\rho^2}\frac{\partial^2\Psi}{\partial\phi^2} = 0. \tag{2.3}$$

Ψ can be re-expressed, as in [2], using the standard separation of variables as a product of functions of ρ and ϕ,

$$\Psi(\rho,\phi) = P(\rho)\Phi(\phi), \tag{2.4}$$

which, when divided into (2.3) and the result multiplied by ρ^2, yields

$$\frac{\rho}{P(\rho)}\frac{d}{d\rho}\left(\rho\frac{dP(\rho)}{d\rho}\right) = -\frac{1}{\Phi(\phi)}\frac{d^2\Phi(\phi)}{d\phi^2}. \tag{2.5}$$

Equation (2.5) can only be true if both sides are equal to a constant, which for convenience we choose m^2, and this leads to both sides being expressed separately as

$$\frac{d}{d\rho}\left(\rho\frac{dP(\rho)}{d\rho}\right) - \frac{m^2}{\rho}P(\rho) = 0 \tag{2.6}$$

$$\frac{d^2\Phi(\phi)}{d\phi^2} + m^2\Phi(\phi) = 0 \tag{2.7}$$

When (2.7) and (2.6) are solved for $\Phi(\phi)$ and $P(\rho)$, respectively, it can be shown that

$$P(\rho) = \begin{cases} C_0^\rho + C_0'^\rho \ln\rho, & m = 0 \\ C_m^\rho\rho^m + \frac{C_m'^\rho}{\rho^m}, & m > 0 \end{cases} \tag{2.8}$$

$$\Phi(\phi) = C_m^\phi\cos(m\phi) + C_m'^\phi\sin(m\phi) \tag{2.9}$$

When (2.9) and (2.8) are combined as required in (2.4), the general solution becomes

$$\Psi(\rho,\phi) = C_0^\rho + C_0'^\rho\ln\rho + \sum_{m=1}^{\infty}\left(C_m^\rho\rho^m + \frac{C_m'^\rho}{\rho^m}\right)\left[C_m^\phi\cos(m\phi) + C_m'^\phi\sin(m\phi)\right]. \tag{2.10}$$

For this particular problem, C_0^ρ must equal zero to guarantee that the electric field approaches a constant as $\rho \to \infty$. Since there is no net charge on the conductor, $C_0'^\rho$ is also zero. In addition, $|\mathbf{E}|$ must approach E_0 as $\rho \to \infty$ and, therefore, m can only equal 1. Finally, since the electric field is directed along the x-axis and the cylinder is located at the central point between the remote sources, the potential along the y-axis must equal 0. As such, the coefficient $C_m'^\phi$ must equal 0. With these conditions defined, the the solution for the potential in regions 2 and 3 can be expressed as

$$\Psi(\rho, \phi) = -\left(K_1 \rho + \frac{K_2}{\rho} \right) \cos \phi. \tag{2.11}$$

Using this solution, the potentials of the three regions, with the conductor of region 1 set to zero potential, can be defined [3] as

$$\Psi_1 = 0. \tag{2.12}$$

$$\Psi_2 = -\left(A\rho + \frac{B}{\rho} \right) \cos \phi, \tag{2.13}$$

$$\Psi_3 = -\left(E_0 \rho + \frac{C}{\rho} \right) \cos \phi, \tag{2.14}$$

2.2.2 Calculation of the electric fields

With the electrostatic potential at each point within the three regions now expressed, the electric field within the three regions can be determined using (2.1), which is expressed in polar coordinates as

$$-\nabla\Psi = -\frac{\partial \Psi}{\partial \rho}\hat{\rho} - \frac{1}{\rho}\frac{\partial \Psi}{\partial \phi}\hat{\phi}. \tag{2.15}$$

Applying this operation to (2.12), (2.13) and (2.14) yields the following respective regional electric fields:

$$\mathbf{E}_1 = 0 \tag{2.16}$$

$$\mathbf{E}_2 = \hat{\rho}\left(A - \frac{B}{\rho^2} \right)\cos\phi - \hat{\phi}\left(A + \frac{B}{\rho^2} \right)\sin\phi \tag{2.17}$$

$$\mathbf{E}_3 = \hat{\rho}\left(E_0 - \frac{C}{\rho^2} \right)\cos\phi - \hat{\phi}\left(E_0 + \frac{C}{\rho^2} \right)\sin\phi \tag{2.18}$$

The coefficients A, B and C contain the geometrical and material properties of the three regions and their effects on the adjacent regions. These can be determined by first applying

the following interface conditions:

$$\Psi_1\bigg|_{\rho=a} = \Psi_2\bigg|_{\rho=a} \tag{2.19}$$

$$\Psi_2\bigg|_{\rho=b} = \Psi_3\bigg|_{\rho=b} \tag{2.20}$$

$$\epsilon_2 E_{2\rho}\bigg|_{\rho=b} = \epsilon_3 E_{3\rho}\bigg|_{\rho=b}, \tag{2.21}$$

which generate the following expressions:

$$A = -\frac{B}{a^2} \tag{2.22}$$

$$Ab + \frac{B}{b} = E_0 b + \frac{C}{b} \tag{2.23}$$

$$\epsilon_2\left(A - \frac{B}{b^2}\right) = \epsilon_3\left(E_0 - \frac{C}{b^2}\right). \tag{2.24}$$

Three equations and three unknowns allows the final calculation of the three unknown coefficients, expressed as

$$A = -E_0 b^2 \frac{2\epsilon_3}{\epsilon_3(a^2 - b^2) - \epsilon_2(a^2 + b^2)} \tag{2.25}$$

$$B = E_0 b^2 \frac{2\epsilon_3 a^2}{\epsilon_3(a^2 - b^2) - \epsilon_2(a^2 + b^2)}. \tag{2.26}$$

$$C = E_0 b^2 \frac{\epsilon_3(a^2 - b^2) + \epsilon_2(a^2 + b^2)}{\epsilon_3(a^2 - b^2) - \epsilon_2(a^2 + b^2)} \tag{2.27}$$

With the three coefficients now known, the electric field intensity can be determined at any point within the three regions.

2.2.3 Numerical evaluation

Suppose an infinite region of air ($\epsilon_{r1} = 1$) is initially influenced by a static electric field intensity of 100 V/m in the x-direction. A cylinder with two concentric regions is then placed with its length along the z-axis of region 3. The inner concentric region, region 1, is an uncharged perfect electrical conductor ($\sigma \to \infty$) with a 5 mm radius while region 2 is a dielectric layer with a 10 mm radius and dielectric constant of 10. To determine the new electric potential and field intensity at any point within the three regions, the coefficients A, B and C must be calculated according to (2.25), (2.26) and (2.27). These are found to be $A = 15.09$, $B = -377.4 \times 10^{-6}$ and $C = -8.867 \times 10^{-3}$.

(a) Vector plot of the electric field   (b) Magnitude of the electric field

Figure 2.2   Cross-section of electric field response to an uncharged dielectric-coated conductive cylinder embedded in a uniform electric field. The uniform field magnitude is 100 V/m. The green and red circles denote the interfaces at $a = 5$ mm and $b = 10$ mm, respectively. For $a \leq \rho \leq b$ the relative permittivity is 10 and for $\rho \geq b$ the relative permittivity is 1.

To verify that these coefficients are correct, one must place the coefficients into the boundary conditions of (2.19), (2.20) and (2.21). It can now be seen that the electrostatic potential at $\rho = a$ is 0, the potentials of regions 2 and 3 are both equal at $\rho = b$, and the normal ($\hat{\rho}$) component of the electric flux density field $\mathbf{D}$ is equal in both regions at the boundary $\rho = b$. Another useful boundary condition check not listed above is the tangential component of the electric field intensity at boundary of regions 2 and 3. One can see that the $\hat{\phi}$-component of $\mathbf{E}$ at $\rho = b$ is equal between the two regions.

With the coefficients A, B and C calculated and the electric field intensity at every point within each region calculated, the electric field now may be plotted in each region, and is shown in Figure 2.2. As can be seen in the plot, the electric field lines appear to be attracted to the outer surface of the cylinder, due to the combined internal properties of the conductor and the dielectric layer, which has a higher permittivity than the surrounding air. The field lines that are obliquely incident upon the dielectric layer are transmitted at a different angle upon entering the dielectric while the single normal line along the x-axis remains normally transmitted. Inside the dielectric, the electric field is less intense at every point than the exterior because of its

higher permittivity. Note that most of the field lines within the dielectric terminate normally upon the surface of the conductor due to the condition at this interface setting the tangential electric field equal to zero. With this configuration, the electric field is most intense at the points $(\rho, \phi) = (10, 0)$ and $(10, \pi)$ with a magnitude of 103.8 V/m.

2.3 Charged dielectric-coated conductive cylinder with zero external electric field

Solving for the electric field generated solely by the charged central conductor involves the same process as in the case of the uncharged central conductor, Section 2.2, with the exception of the absence of the external electric field and the introduction of a constant potential Φ_C in region 1. With the absence of the external electric field, the potential in (2.10) now has complete circular symmetry, resulting in $C_m^\phi = C_m'^\phi$ and the elimination of the dependence of the potential on ϕ. Therefore, the general solution of the potential for the uncharged cylinder becomes

$$\Psi(\rho) = K_1\rho + \frac{K_2}{\rho}. \tag{2.28}$$

As $\rho \to \infty$, K_1 must equal zero for region 3. Because there are three regions that require definition of the potentials, these potentials should have the form

$$\Psi_1 = \Phi_C \tag{2.29}$$

$$\Psi_2 = L\rho + \frac{M}{\rho} \tag{2.30}$$

$$\Psi_3 = \frac{N}{\rho} \tag{2.31}$$

By (2.1), the electric fields can then be expressed as

$$\mathbf{E}_1 = 0 \tag{2.32}$$

$$\mathbf{E}_2 = \hat{\rho}\left(\frac{M}{\rho^2} - L\right) \tag{2.33}$$

$$\mathbf{E}_3 = \hat{\rho}\frac{N}{\rho^2}, \tag{2.34}$$

(a) Vector plot of the electric field   (b) Magnitude of the electric field
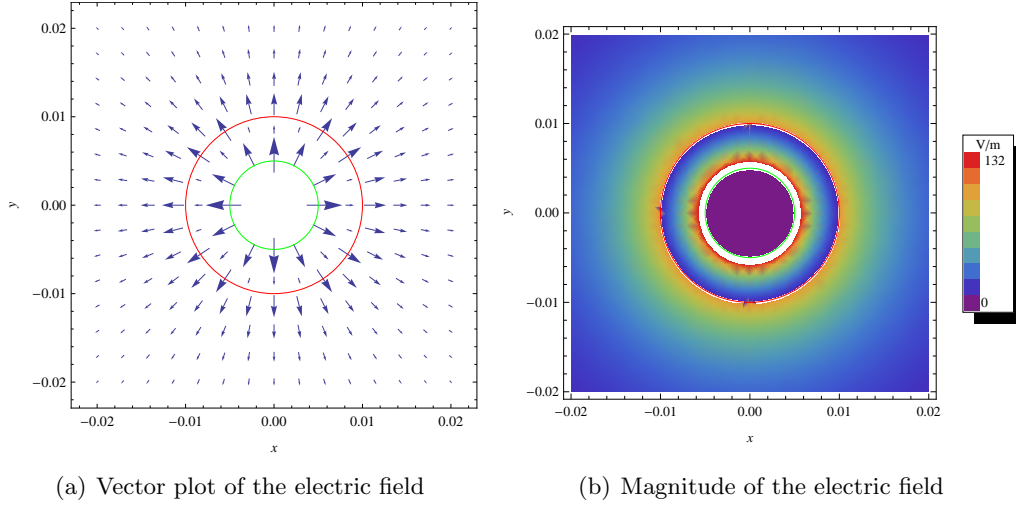
Figure 2.3   Cross-section of electric field generated by a charged dielectric-coated conductive cylinder embedded in an air region. The potential of the conductor in the region $\rho < a$ is 1 V. The green and red circles denote the interfaces at $a = 5$ mm and $b = 10$ mm, respectively. For $a \leq \rho \leq b$ the relative permittivity is 10 and for $\rho \geq b$ the relative permittivity is 1.

where the coefficients L, M and N can be solved for using the interface conditions in (2.19), (2.20) and (2.21):

$$L = a\Phi_C \frac{\epsilon_3 - \epsilon_2}{\epsilon_3(a^2 - b^2) - \epsilon_2(a^2 + b^2)} \tag{2.35}$$

$$M = -ab^2\Phi_C \frac{\epsilon_3 + \epsilon_2}{\epsilon_3(a^2 - b^2) - \epsilon_2(a^2 + b^2)} \tag{2.36}$$

$$N = -2ab^2\Phi_C \frac{\epsilon_2}{\epsilon_3(a^2 - b^2) - \epsilon_2(a^2 + b^2)} \tag{2.37}$$

For the same cylinder with the same parameters as in the uncharged cylinder case and with $\Phi_C = 1$ V, the charged cylinder constants are evaluated as $L = 33.96$, $M = 4.151 \times 10^{-3}$ and $N = 7.547 \times 10^{-3}$. Vector and magnitude plots of the electric field are shown in Figure 2.3. It is worth noting from the figure that the electric field is strongest just outside the interface $\rho = a$, with a value of 132.1 V/m, as should be expected. Within the dielectric layer, the electric field decays toward a value of 7.547 V/m as $\rho \to b$, but just beyond the interface at $\rho = b$ the electric field experiences a jump to 75.47 V/m due to the dielectric discontinuity.

2.4 Charged dielectric-coated conductive cylinder embedded in a uniform electric field

With the external field response to the uncharged cylinder, Section 2.2, and the generated field from the charged cylinder, Section 2.3, completely determined at every point, the two fields can now be superimposed to yield the total electric field. The field expressions for the three regions now hold the final form of

$$\mathbf{E}_1 = 0 \tag{2.38}$$

$$\mathbf{E}_2 = \hat{\rho} \left[\left(A - \frac{B}{\rho^2} \right) \cos\phi + \frac{M}{\rho^2} - L \right] - \hat{\phi} \left(A + \frac{B}{\rho^2} \right) \sin\phi \tag{2.39}$$

$$\mathbf{E}_3 = \hat{\rho} \left[\left(E_0 - \frac{C}{\rho^2} \right) \cos\phi + \frac{N}{\rho^2} \right] - \hat{\phi} \left(E_0 + \frac{C}{\rho^2} \right) \sin\phi. \tag{2.40}$$

Figure 2.4 shows vector and magnitude plots of the total electric field for a cylinder with $a = 5$ m, $b = 10$ m, $\epsilon_{r2} = 10$, and $\Phi_C = 1$ V embedded in an air space with $\epsilon_{r3} = 1$ and $E_0 = 100$ V/m directed in the x-direction. It may now be easily seen that the introduction of an electric potential on the central conductor will imbalance the magnitude of the electric fields between both sides of the y-axis. This is because the fields generated by the conductor in the positive x-region constructively combine with those of the external field while those in the negative x-region deconstructively combine. There is now a single maximum of the electric field occurring in region 3 at $(\rho,\phi) = (10,0)$ with a value of 179.3 V/m.

2.5 Effect of charged central conductor on the capacitance

In order to understand the effect of a charged central conductor on the capacitance of two patch electrodes, discussed further in Section 3.3.1, that are in contact with opposite sides of a wire, a simplified analysis is performed here that relies upon the cross-sectional symmetry of the electrode configuration. Because of the cross-sectional physical symmetry of the wire and electrodes, the electrostatic behavior of the system can be illustrated by a thought-experiment in which two parallel-plate capacitors are connected in series, with a variable center voltage, as shown in Figure 2.5.

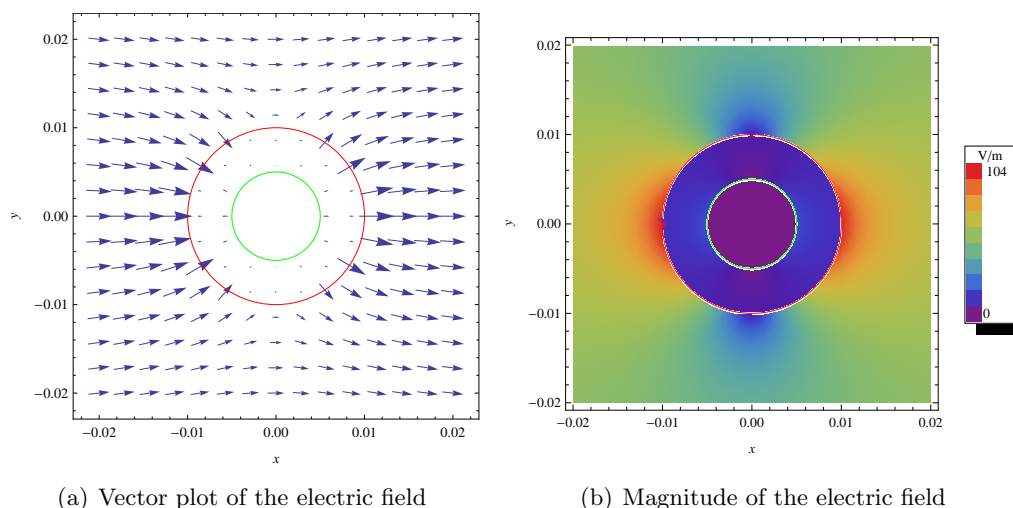(a) Vector plot of the electric field

(b) Magnitude of the electric field
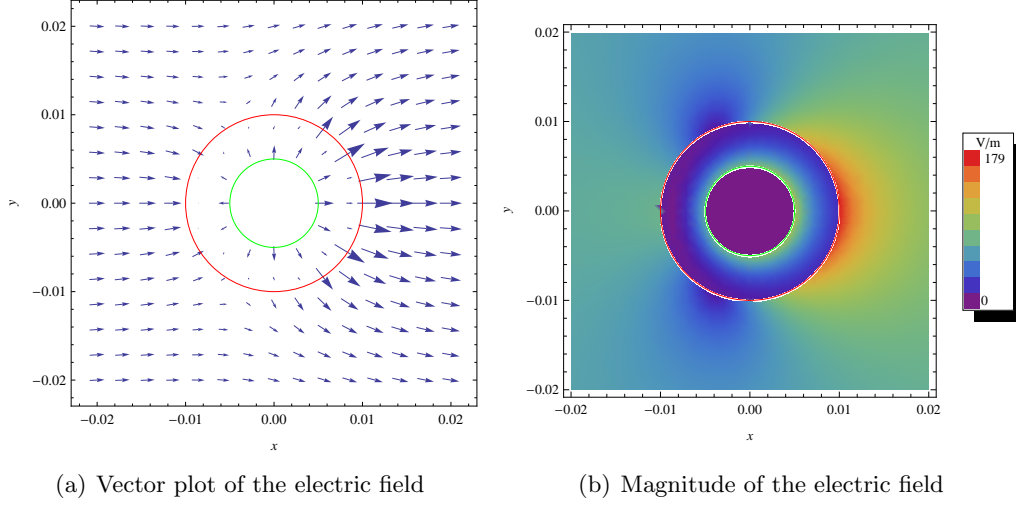
Figure 2.4   Cross-section of electric field generated by a charged dielectric-coated conductive cylinder embedded in a uniform electric field. The potential of the conductor in the region $\rho < a$ is 1 V and the uniform field has an intensity of 100 V/m. The green and red circles denote the interfaces at $a = 5$ mm and $b = 10$ mm, respectively. For $a \leq \rho \leq b$ the relative permittivity is 10 and for $\rho \geq b$ the relative permittivity is 1.

The voltages V_U and V_L represent those on the upper and lower curved patch electrodes, respectively, applied to the dielectric insulation layer of a wire. The voltage V_C represents the voltage on the wire central conductor. The total capacitance C_T of the system can be described as two capacitors connected in series, defined as

$$C_T = \frac{1}{\frac{1}{C_1} + \frac{1}{C_2}}, \tag{2.41}$$

where C_1 and C_2 are the capacitances of the upper and lower pairs of parallel plates, respectively, shown in Figure 2.5. Each parallel plate capacitance is also given by the general charge separation equation

$$C_i = \frac{Q_i}{V_i}, \qquad i = 1, 2 \tag{2.42}$$

where Q is the total charge of each capacitor and V is the voltage between the plates. Each capacitance can then be defined as

$$C_1 = \frac{Q_1}{V_1} = \frac{Q_1}{|V_U - V_C|} \tag{2.43}$$
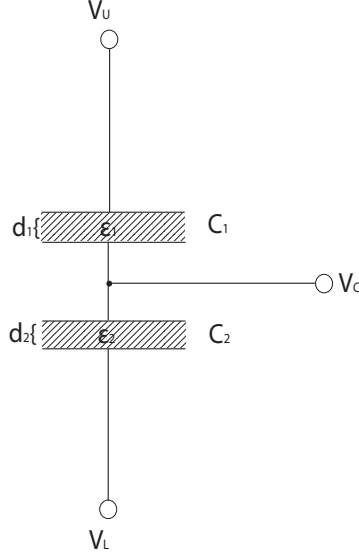
Figure 2.5   Two capacitors, C_1 and C_2, in series with a variable center voltage V_C.

and

$$C_2 = \frac{Q_2}{V_2} = \frac{Q_2}{|V_L - V_C|}. \tag{2.44}$$

Substituting these relationships into (2.41),

$$C_T = \frac{1}{\frac{V_1}{Q_1} + \frac{V_2}{Q_2}}. \tag{2.45}$$

From this equation, it is apparent that the voltages depend upon V_C but the charges remain unknown. One can find the general charge solution by utilizing Gauss' law, defined as

$$Q = \oiint \mathbf{D} \cdot d\mathbf{S} = \epsilon \oiint \mathbf{E} \cdot d\mathbf{S}, \tag{2.46}$$

where $\mathbf{D}$ is the electric flux density, $\mathbf{E}$ is the electric field intensity, $d\mathbf{S}$ is a differential surface element of the plates, and ϵ is the permittivity of the dielectric between the plates, which is assumed to be the same for both capacitors. Assuming no fringing fields, the magnitude of both $\mathbf{D}$ and $\mathbf{E}$ are uniform in the volume between the plates, such that

$$|\mathbf{D}| = \epsilon |\mathbf{E}| = \epsilon \nabla V = \epsilon \frac{V}{d}, \tag{2.47}$$

where d is the distance of separation between the plates, and by substituting this relationship into (2.46), the charge Q for each capacitor becomes

$$Q_i = \epsilon_i A_i \frac{V_i}{d_i}, \qquad i = 1, 2. \tag{2.48}$$

Finally, one can use this definition of the charge in (2.45) as

$$C_T = \frac{1}{\frac{V_1}{\frac{\epsilon_1 A_1 V_1}{d_1}} + \frac{V_2}{\frac{\epsilon_2 A_2 V_2}{d_2}}} = \frac{\epsilon_1 \epsilon_2 A_1 A_2}{\epsilon_1 d_2 A_1 + \epsilon_2 d_1 A_2}, \tag{2.49}$$

where ϵ_1 and ϵ_2 are the permittivity values, A_1 and A_2 are the plate areas, and d_1 and d_2 are the plate separations of the upper and lower capacitors, respectively. As is seen in (2.49), a variable central conductor voltage will have no effect on the total capacitance of the system due to the fact that the charge is a function of the applied voltage, which is canceled out of the relationship and leaves only the permittivity, area, and plate separation dependencies. This is an important piece of information for real-world capacitance measurements onboard aircraft in that wires need not be de-energized for an accurate reading.

2.6   References

[1] T. Chen and N. Bowler, "Analysis of a capacitve sensor for the evaluation of circular cylinders with a conductive core", *Meas. Sci. Technol.*, Vol. 23, 045102(10pp), 2012.

[2] M. N. O. Sadiku, *Elements of Electromagnetics*, 5th ed. New York: Oxford, 2010.

[3] É. Durand, *Électrostatique et magnétostatique*, Paris: Masson et cie, 1953.

CHAPTER 3.   WIRE TEST SPECIMEN CHARACTERIZATION USING RESISTANCE AND CAPACITANCE MEASUREMENTS

3.1   Introduction

Insulation testers are among the most common instruments currently used to determine the viability of wire insulation. A current-carrying wire is usually a good conductor, typically copper or aluminum, enclosed by one or several protective insulation layers, which are exposed to the outside world. As such, no insulation layer is a perfect insulator and becomes even less so over time due to the presence of extreme temperatures, moisture, and corrosive chemicals. For certain types of degradation, the insulation can actually become more conductive to free charges, leading to a potentially dangerous situation in critical systems, such as aircraft, where an electrical arc can jump through the degraded insulation from the wire conductor to another conductor of differing potential, which can cause system shutdowns or fires.

According to [1], applying a voltage step across a segment of wire insulation results in the flow of a current through the insulation that can be decomposed into three components, as shown in Figure 3.1:

1. *Capacitance charging current* - initially high and decays to zero after a few milliseconds; depends upon permittivity, area of electrode contacts, and thickness of insulation.

2. *Absorption current* - also initially high and decays to zero after the charging current has significantly decayed; the result of a lossy dielectric medium [2].

3. *Leakage current* - initially zero and tends to a constant value once the charging and absorption currents have vanished; depends upon the conductivity of the insulation.

These individual currents are not easily discriminated by most insulation testers and, as a
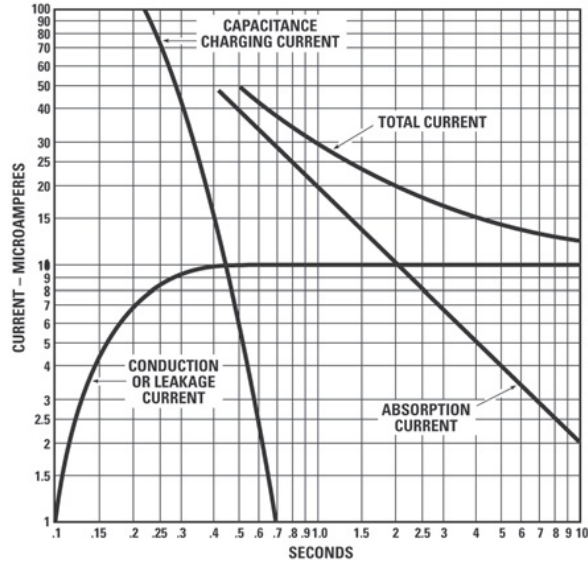
Figure 3.1   Component currents that flow through wire insulation during a typical resistance test [1].

result, are measured by the tester as a summation of the three, taking the form of a current that is initially high and eventually converges to the steady-state leakage current value.

Although this type of testing is not suitable for the testing of wires onboard an aircraft, due to the requirement of having access to the central conductor, a study was performed for purposes of assessing the quality of information that could be obtained from a standard, off-the-shelf tester. The associated resistance of the total leakage current was measured for 17 wire samples retrieved from a retired aircraft, the specifications of which are given in Tables 3.1 and 3.2. A photo of a selection of these wires is given in Figure 3.2. The details of this experiment are described in Section 3.2.

Although insulation testers are readily available on the commercial market to test wire insulation resistance, a function of the conductivity, there are no products known to determine the permittivity of wire insulation, the other key electrical and material property of insulation. Because capacitance is directly related to permittivity, a capacitive sensor is therefore an ideal choice for determining degradation effects on the insulation permittivity. Capacitance measurements using curved patch electrodes were performed on the same 17 wire samples and the experiments of which are described in Section 3.3.

Table 3.1 Dimensions and insulation layer material of three different gauge aircraft wires of type BMS-13-5.

Material		20 (AWG)	18 (AWG)	16 (AWG)
Copper diameter	(mm)	0.9906 ± 0.051	1.2319 ± 0.064	1.3970 ± 0.076
PVC thickness	(mm)	0.2159 ± 0.025	0.2191 ± 0.025	0.2413 ± 0.025
Glass braid thickness	(mm)	0.2159 ± 0.025	0.2191 ± 0.025	0.2413 ± 0.025
Nylon thickness	(mm)	0.1524 ± 0.025	0.1524 ± 0.025	0.1524 ± 0.025
Overall Diameter	(mm)	2.159 ± 0.127	2.413 ± 0.127	2.667 ± 0.127

Figure 3.2 Photo of a selection of the 17 wire specimens. From left to right: wires I, M and A. Note the severe discoloration in wire A, which was found to have been highly degraded.

3.2   Insulation resistance tests

A Megger® MIT 510 insulation tester was used to perform two types of tests, each described in Sections 3.2.1 and 3.2.2, on 17 wire specimens provided by the project sponsor. Each test was performed with one electrode clamped to the central conductor at all times while the other electrode was clamped partially around the insulation, as shown in Figure 3.3.

3.2.1   Insulation resistance - single-measurement testing

An instantaneous value of insulation resistance can be measured as part of the standard insulation resistance test. On each wire, measurements were made at 20 different locations, after 60 seconds of applying approximately 5.1 kV. At 60 s, the resistance has generally approached a constant value that is inversely proportional to the leakage current through the insulation at

Table 3.2 Descriptions and locations of 17 wire specimens of type BMS-13-5 removed from a single retired aircraft. Note that AWG is the American Wire Gauge, a standard unit of diameter. In this case, 20 AWG = 2.159 mm, 18 AWG = 2.413 mm and 16 AWG = 2.667 mm.

Wire label	Specimen #	Gauge (AWG)	Aircraft Location	Qualitative Description
A B C	2	20	Right-hand aft landing gear	Very brittle, yellow-brown Very brittle, brown Very brittle, yellow
D	4	20	Between forward pressure bkhd & left wing station 230	Slightly dirty, flexible, white
E F G H	5	20	Forward pressure bulkhead, unpressurized side	Slightly dirty, flexible, white
I J K	6	20	Between right front spar and strut break	Clean, flexible, white
L	16	16	Between forward pressure bulkhead & right rear spar	Slightly off-white
M	23	18	Between strut break & engine #2 firewall	Very dirty, flexible, off-white
N	24	18	Unpressurized fuselage aft of forward pressure bkhd	Clean, slightly discolored
O P Q	27	20	Between station 1179 & rudder actuator	Dirty, slightly discolored

the measurement point. For 10 measurements, the outer clamp electrode was moved along one line parallel to the wire axis (i.e., at azimuthal angle $\phi = 0°$). For 10 further measurements, the wire was rotated 90° and the procedure repeated. Reported results are the mean and one standard deviation of these 20 measurements, shown in Figure 3.4. Wire specimen details are listed in Table 3.2.

The most obvious observation from the data in Figure 3.4 is the extremely low resistance values of wires A and B, both from specimen 2, which matches the qualitative observation of the wires during testing, that all three wires from specimen 2 were extremely brittle, were significantly discolored, and appeared to be in the poorest condition when compared to the other specimens. It is also important to note that the standard deviation of the measurements,
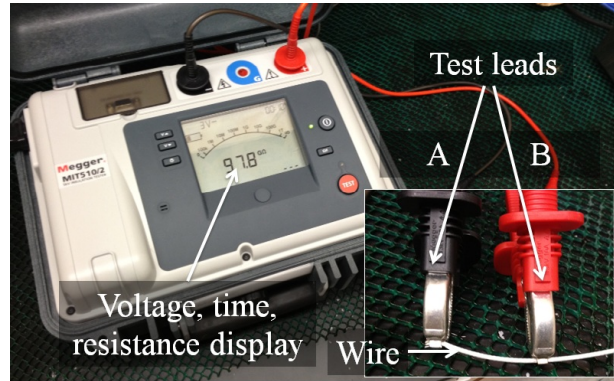
Figure 3.3 Experimental configuration for wire insulation tests with a Megger® MIT 510 insulation tester. Test lead A clamps around the central conductor of the wire while test lead B clamps around the outer insulation.

in this case, represents how much of the wire was in a specific condition. For example, wire C had a higher mean resistance than the others in its specimen group, but the measurement showed a large standard deviation, meaning the wire had some very "good" areas of insulation and also very "poor" areas. Another point of important note is that the maximum measurable resistance of the MIT 510 is 15 TΩ. Many of the resistance values taken during this test were actually above this level, which prevents a measurable reading and therefore affects the reliability of the displayed data in Figure 3.4. This issue is most apparent in wires D and M, which consistently had values above 15 TΩ, and, as such, the zero standard deviation is misleading. It can be deduced that, among this group of specimens, these two wires had the lowest conductivity within the insulation layer.

3.2.2 Insulation resistance - timed testing

The *dielectric absorption ratio*, or DAR, as defined in [1], is the ratio of the insulation resistance values at 60 s to those at 30 s. This ratio generally characterizes the absorption current that flows through the insulation in the initial moments after application of the test voltage. The DAR value essentially represents the ratio of the resistance associated with the sum of the absorption and leakage currents at 60 s to that associated with solely the leakage current at 30 s, which should increase during that time period, according to Figure 3.1. DAR values of 1.0 to 1.2 indicate "questionable" insulators while values above 1.6 indicate "excellent"
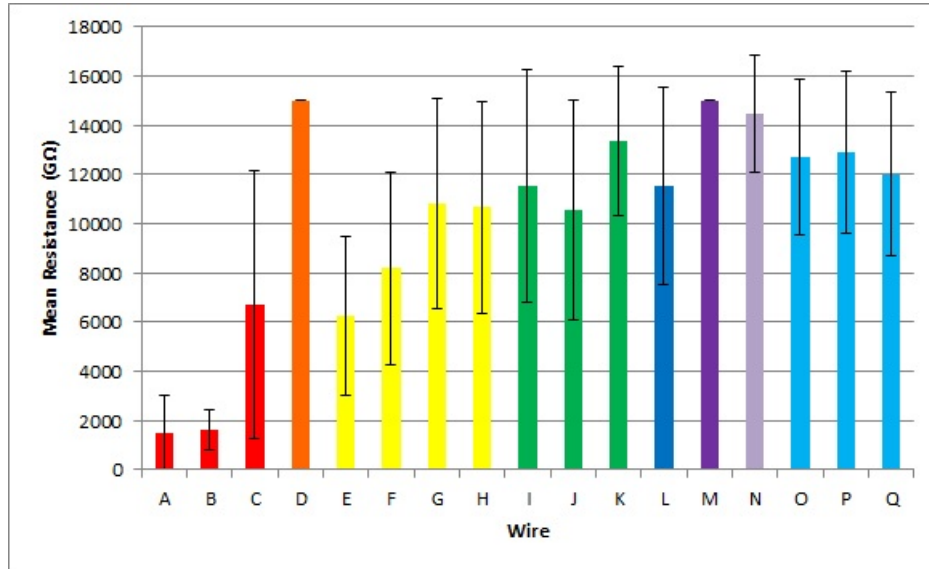
Figure 3.4   Resistance of wire samples at 60 s. The resistance level of each wire shown is the
average of the 20 points tested and the error bar represents ±1 standard deviation
of the 20 measurements. Wires D and M had all 20 measurement points out of the
15 TΩ range of the insulation tester, thus explaining the zero standard deviation.

insulation performance [1].

Measured DAR results are shown in Figure 3.5, again with each data column plotted as the
average of 20 measurements with a ±1 standard deviation error bar. In this test, the resistance
of many samples, especially at the 60 s measurement, exceeded the maximum 15 TΩ measurable
by the MIT 510. For this reason, DAR results for only five wires, comprising specimens 2 and
5, are shown. The DAR values for wires A and B, specimen 2, are low, between 1.0 and 1.2.
Hence, these would be classified as "questionable" insulators, as the resistance increased very
little between 30 s and 60 s. This result correlates with the findings of the standard resistance
measurement, shown in Figure 3.4. Wires C, E and F showed slightly higher DAR values,
between 1.2 and 1.3, which also correlate with the standard resistance test results. Accurate
DAR values for the better insulators may be obtained with a different insulation tester that
can apply a voltage higher than 5 kV and has the capability of measuring resistance values
greater than 15 TΩ.
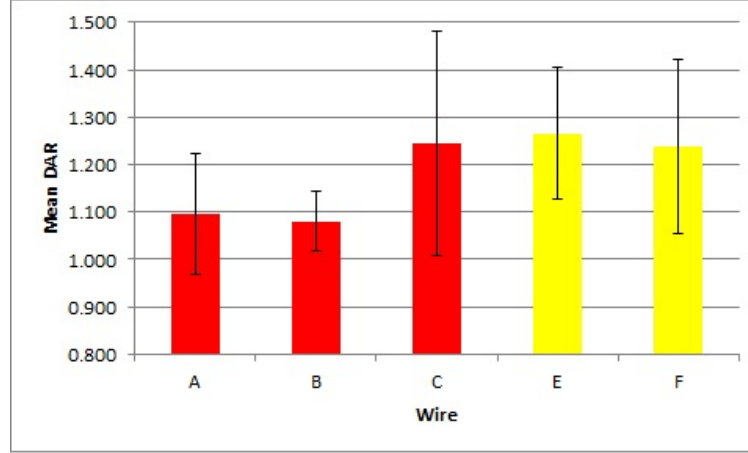
Figure 3.5   Dielectric absorption ratio (DAR) - the ratio of the resistance at 30 s to that at
             60 s. The DAR of each wire shown is the average of the 20 points tested and the
             error bar is ±1 standard deviation of the 20 measurements.

3.3   Capacitance measurements using curved patch-electrodes

For this experiment, the curved patch-electrode sensor presented in [3] is adopted as the
preferred insulation characterization method. Figure 3.6 shows the basic concept of the design,
which is composed of two conducting electrodes, each with length l in the in the longitudinal
direction and arc width w in the azimuthal direction.

Although the sensor is designed to measure capacitance, a function of the insulation per-
mittivity, real insulation is not a perfect insulator, as discussed in Chapter 1. Dissipation factor
D, also known as *loss tangent*, is the ratio of the imaginary component to the real component
of the complex permittivity,

$$D = \tan\delta = \frac{\sigma}{\omega\epsilon'}. \tag{3.1}$$

In capacitive measurements performed by an LCR meter, the dissipation factor is the ratio of
the real, or resistive, component of the impedance to the imaginary, or reactive, component.
This resistive component is known as the equivalent series resistance and is not simply the
resistance through the insulation because it depends on frequency, the real permittivity and the
real capacitance. Since research in [4] has shown that the imaginary component of permittivity
correlates with the level of degradation, the dissipation factor is conjointly measured with the
capacitance in this experiment.
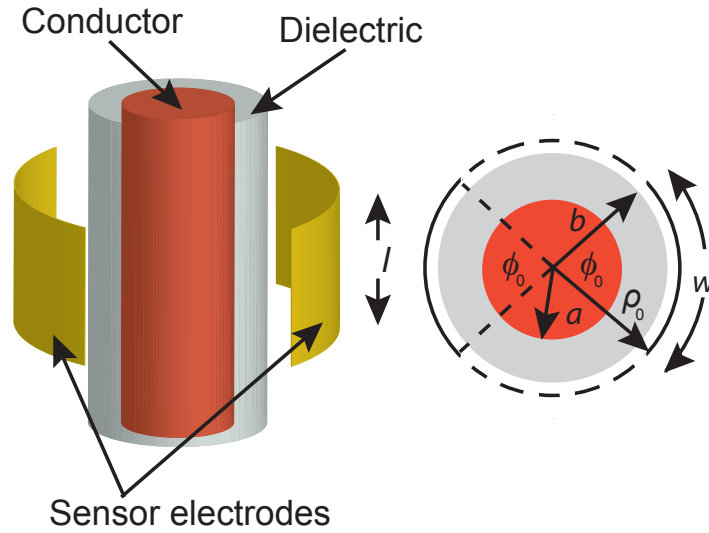
Figure 3.6   Curved patch-electrode capacitive sensor [3]. Electrode, central conductor and insulation radii are denoted as ρ_0, a and b, respectively. Each electrode has length l and arc-width $w = \phi_0 \times \rho_0$, where ϕ_0 is the electrode arc-angle.

3.3.1   Capacitive experiments

A patch-electrode test fixture, shown in Figure 3.7, was designed to support the two electrodes for the purpose of making measurements on aircraft wires of three different gauges, the parameters of which are shown in Table 3.1. Arc-shaped grooves were milled from the surface of a pair of 20-mm-long Perspex® acrylic blocks, with one groove for each gauge of wire. To ensure that each groove would leave enough room for the electrodes and allow for changes in the wire shape due to deterioration, the diameters for the 20 AWG, 18 AWG and 16 AWG wires were oversized by one milling bit size above the diameters of the wires to 2.184 mm, 2.438 mm and 2.705 mm, respectively.

A distance of 0.96 mm was designed as the spacing between the plates when fully clamped around any of the wires although, as will be described later, this distance greatly depended on the varying size of the actual wire. Conductive pins were fitted through the acrylic plates to make contact with the surface of the grooves. The surface of each groove was coated with a layer of silver paint to act as the curved patch-electrodes and making electrical contact with the pins.
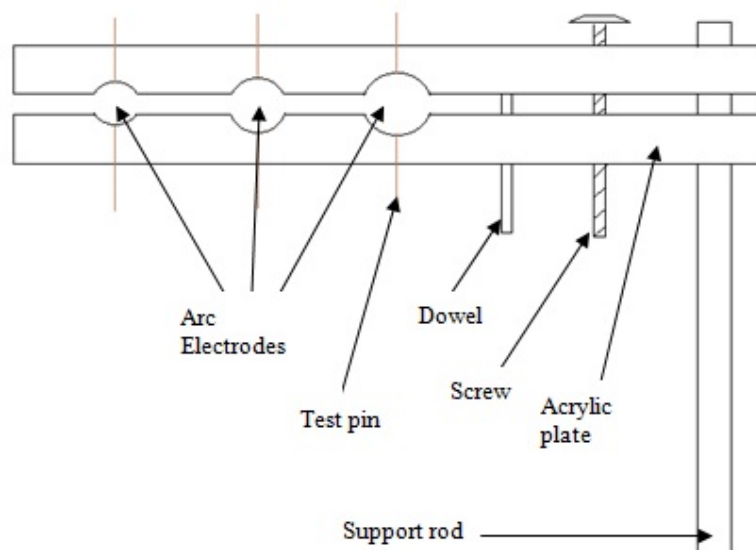
Figure 3.7   Side view design plan of the curved patch-electrode test fixture.

As with the insulation resistance tests, each of the 17 wire samples, described in Table 3.2, were measured at 20 different points, with 10 measurements along the longitudinal axis at angle ϕ and another 10 taken at $\phi + 90°$. The capacitance and dissipation factor measurements were taken using an Agilent E4980A Precision LCR meter with a connected Agilent probe test fixture 16095A at an operating frequency of 1 MHz, each recorded measurement being the average of 16 measured values computed by the LCR meter. An alternating current at 1 MHz can be used in these measurements to approximate ideal direct current conditions because the associated wavelength in free space is much larger than the length of the actual sensor. The LCR meter was calibrated before taking the measurements to remove the resistive and reactive contributions from the meter itself and from the connecting cable. This was completed using the standard calibration procedure of placing a short and open across the leads of the probe and setting those values in the LCR memory. Although it was intended to keep the plate separation constant for this experiment, the widely-varying (and, in the case of specimen 2, larger) diameters of the wires, which resulted from degradation, prevented consistent plate separations. Instead, the acrylic plates were compressed for minimal plate separation so that each patch electrode was made to be in as much intimate contact with the wire sample as possible and the resulting plate separation was measured in each case. The results of the
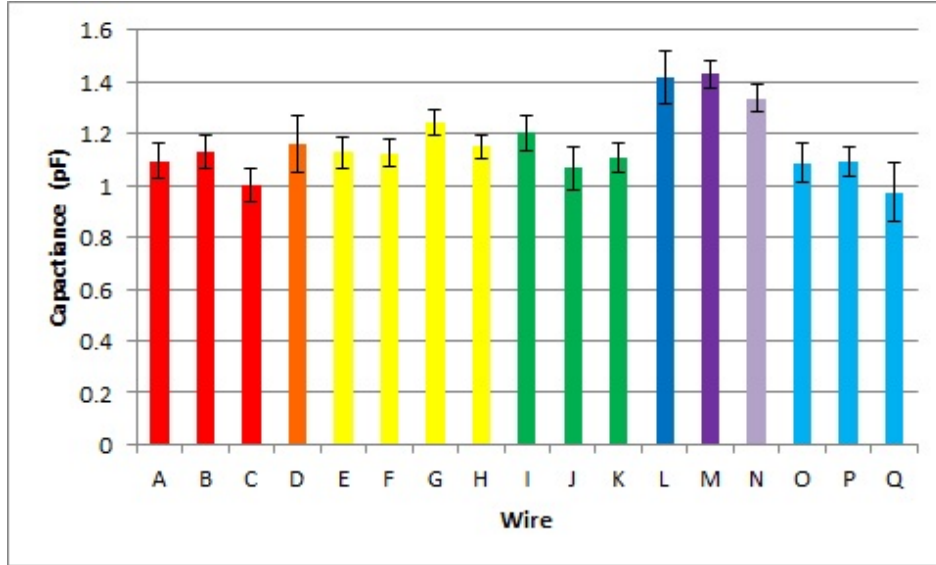
Figure 3.8   Capacitance of the wire samples measured using the curved patch-electrode sensors. The capacitance of each wire shown is the average of the 20 points tested and the error bar is ±1 standard deviation of the measurements.

capacitance and dissipation factor experiments are given in Figures 3.8 and 3.9, respectively. The measured acrylic plate separations are given in Figure 3.10.

Though the capacitance results in Figure 3.8 do not clearly indicate damage, as expected since other work in [4] suggest that degradation affects ϵ' by only a few percent, this is most likely the effect of the variations in the plate separations. Wires A, B and C have 9% lower capacitance values yet also have the 30% larger plate separations than for the remaining wires, the effect of which may be masking changes in ϵ'. The capacitance results also validate patch-electrode numerical simulations in [3] that have shown that larger conductor diameters relative to a constant outer dielectric radius result in larger capacitance. This effect is apparent in wires L, M and N, which have relatively larger conductor diameters than those of the remaining wires.

The dissipation factor D in Figure 3.9 was expected to increase with greater degradation, because the numerator of its ratio is proportional to ϵ'', which has been shown in [4] to be one key indicator of insulation degradation, increasing significantly with heat damage. The data taken from this experiment once again demonstrate that specimen 2 has degraded significantly when compared to the other wires, not only because D for specimen 2 is 48% higher than for the others, but the measured standard deviation is much larger, which in this case indicates
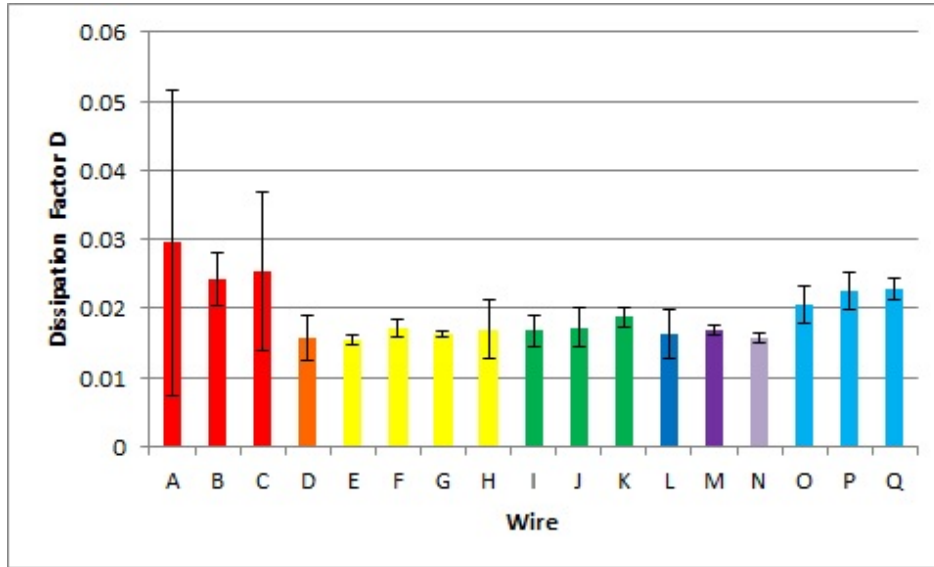
Figure 3.9   Dissipation factor of the wire samples using the curved patch-electrode sensors. The dissipation factor level of each wire shown is the average of the 20 points tested and the error bar is ±1 standard deviation of the measurements.

the magnitude of degradation as a function of position. As such, the dissipation factor data reflect the same trend as the insulation resistance tester results given in Chapter 2.

Finally, it is important to discuss the statistical spread of the sensor plate separations s, as indicated in Figure 3.7, when taking the capacitance measurements. In an ideal testing scenario, the sensor would have been in complete intimate contact with the wire, leaving a 0.96 mm separation between the two acrylic plates. However, as shown in Figure 3.10, the greatly expanded diameters of specimen 2, most likely a result of degradation, prevented the attainment of the 0.96 mm goal, though the patch-electrodes could still enclose a majority of the wire. The average plate separation of wires E through Q was 0.85 mm while for wires A through C this was 1.1 mm, which is 30% higher than that of the other wires. This means that the capacitance measurements may have been more sensitive to plate separation than to permittivity changes while the dissipation factor differences in these two groups of wires are far higher than 30% and still hold value in showing degradation changes in the permittivity.
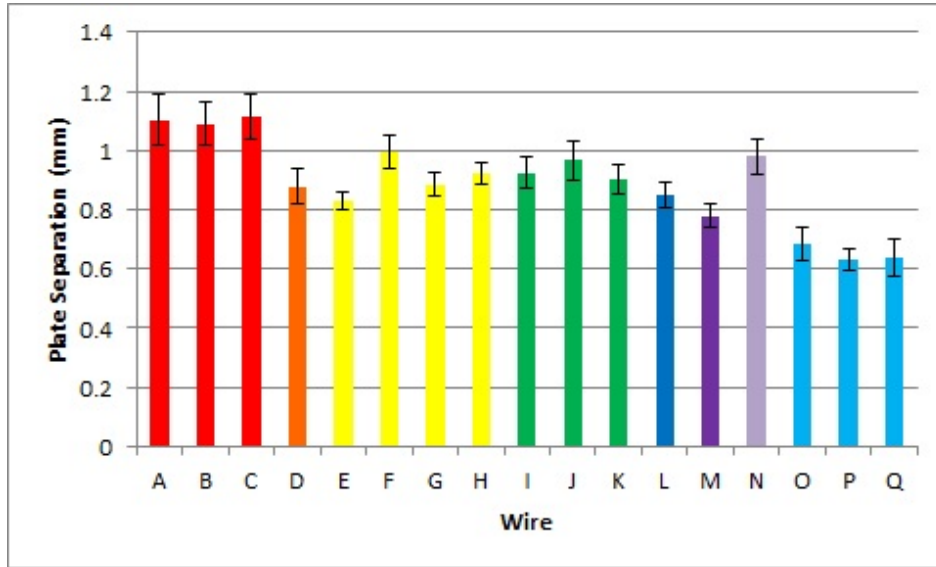
Figure 3.10   Measured sensor plate separation for each wire sample. The separation level of
each wire shown is the average of the 20 points tested and the error bar is ±1
standard deviation of the measurements.

3.4   Conclusion

Based on the results of the resistance tests, it may be concluded that standard insulation resistance tests give a reasonable quantitative indication of wire insulation degradation. It is also possible that DAR tests are good indicators of degradation, but testers with higher voltage and resistance thresholds would be required for a definitive answer. It should be noted that the resistance data appears to correlate closely with the visible and physical condition of the wires. Apparent brittleness also appears to be a better indicator of poor insulation performance than discoloration.

Capacitive sensors, in this case the curved patch-electrode sensor, do indeed indicate levels of degradation in the form of increased dissipation factor. The standard deviation of these measurements also indicates the existence of localized regions of degradation of various magnitudes. Degradation was also found to have swollen the diameters of the affected wires, which requires any future sensor design of this type to adapt to keep the electrode plate separation as consistent as possible between measurements. One final observation is the very low level of the capacitance measurements in Figure 3.8, approximately 1 pF. Values this small are highly

susceptible to noise and are difficult to measure accurately by the LCR meter. This provides motivation for progressing to a sensor design utilizing interdigital electrodes, as discussed in the next chapter.

3.5   References

[1] *A Stitch in Time: The Complete Guide to Electrical Insulation Testing.* Dallas: Megger, 2006.

[2] X. Qi and S. Boggs, "Absorption Current vs. Charge Voltage for Industrial Quality Capacitors", *Conference Record of the 2006 IEEE International Symposium on Electrical Insulation*, pp. 277-280, 2006.

[3] T. Chen and N. Bowler, "Analysis of a capacitve sensor for the evaluation of circular cylinders with a conductive core", *Meas. Sci. Technol.*, Vol. 23, 045102(10pp), 2012.

[4] L. Li, "Dielectric properties of aged polymers and nanocomposites", *Theses and Dissertations*, Paper 12128, Iowa State University, 2011.

CHAPTER 4. A CYLINDRICAL INTERDIGITAL CAPACITIVE SENSOR FOR DIELECTRIC CHARACTERIZATION OF WIRE INSULATION

4.1 Introduction

Results from the curved patch-electrode experiments in Chapter 3 have indeed shown that degradation affects the insulation of wires in quantities measurable by a sensor that is, in fact, simply a capacitor. From the general equation of a parallel plate capacitor, $C = \epsilon A/d$, the most basic capacitor requires two electrodes with area A separated by a distance d with a material of permittivity ϵ in between the electrodes. The patch-electrode sensor is, essentially, a parallel plate capacitor that conforms to the surface of a cylinder with a conductive layer in the middle of the dielectric. The problem with this design, however, is that in order to increase the measurable capacitance, which minimizes the measurement error, for a given dielectric material, d must be decreased and/or A must be increased, which significantly decreases the volume of insulation being sensed. A capacitance value in the range offered by the patch-electrode configuration is susceptible to noise and falls within an accuracy range of the LCR meter, approximately 0.3%, that is less than the optimal 0.1% [1].

The curved patch-electrode configuration also suffers from a disadvantage in which the electric field is primarily concentrated in the gaps between the two electrodes, thus restricting the sensitivity to these two relatively small regions. For example, if degradation is highly localized, as was shown to be common in Chapter 3, the ability to detect small regions of degradation would highly depend on the patch-electrode sensor's azimuthal position. This disadvantage can be significantly alleviated by replacing the patch-electrodes with an array of interdigital electrodes, which increases the total volume of insulation being sensed. As

mentioned in Chapter 1, an array of "interdigital" electrodes[1] greatly multiplies the capacitance of a single pair. Using the principle that the curved patch-electrodes conform to the surface of a wire, the interdigital electrodes are conformed as well, and it is this concept that initiated the research in the following sections.

This new cylindrical interdigital capacitive sensor also mitigates the problem of the variable plate separation for wires of varying diameter, as discussed in Section 3.3.1. Most digit pairs are separated by a fixed distance because they are permanently deposited to the flexible electrode substrate. This means that the capacitance will not be significantly affected by a varying wire diameter, allowing a more accurate comparison of wires of similar construction.

In this chapter, a theoretical model is developed to calculate the capacitance of a cylindrical interdigital sensor that combines the advantages of a coplanar interdigital array with the convenient cylindrical geometry of the curved patch-electrodes. This new cylindrical interdigital sensor offers the improvement over the curved patch-electrodes that: a greater region of the dielectric layer is sensed, the signal-to-noise ratio is substantially higher, and sensitivity to permittivity changes is easily tunable. A method for optimizing the sensor penetration depth is presented and benchmark experimental results show agreement with the numerical model to within 5%.

4.2 Modeling

4.2.1 Sensor configuration

Figure 4.1 shows a perspective view of the configuration of the capacitive sensor. As this sensor is designed to be affixed to two separate faces of a clamp that conforms to opposite sides of a wire, the individual electrode digits are periodically spaced only around a half circumference of the wire and exist on the other half circumference in mirrored positions yet opposing polarity. Each half of the sensor is composed of N_E positive or negative digits enclosed by $N_E + 1$ negative or positive digits, guaranteeing an odd number of digits per half of the sensor and an even number of total digits, defined, therefore, as $N_{ET} = 4N_E + 2$. For one half of the sensor,

---

[1]The interdigital sensor is comprised of two *electrodes* of opposite polarity that are each divided into a number of *digits*.
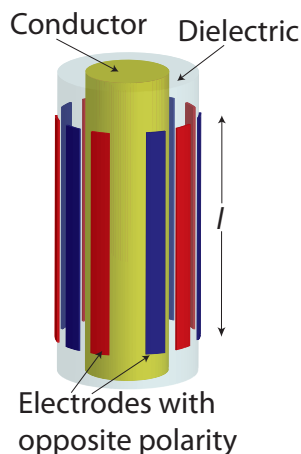
Figure 4.1   Cylindrical interdigital capacitive sensor configuration used in numerical modeling. Blue and red electrodes indicate opposing polarity. Electrodes are interconnected in practice, as shown in Figure 4.2.

each electrode has an arc-width w and arc-spacing s in the ϕ-direction, and length l in the z-direction. There are, therefore, two gaps g that occur between the end digits of each half of the sensor, which represent the discontinuity in full circumferential periodicity of the digits that is likely to occur in the actual sensing clamp, and is given by $g = \pi c - w - 2N_E(s + w)$. To charge each of the electrodes in the experiments discussed in Section 4.5, a thin 0.1 mm power bus connects all positive electrodes together and all negative electrodes together. The power bus, shown in Figure 4.2, is thinner than any of the electrodes and separated from the digits by spacing somewhat greater than the electrode spacings s in order to reduce any stray capacitance contribution to the overall measurement.

    In the theoretical model, the wire itself is modeled as a cylinder that is infinitely long and comprised of a central perfect conductor of radius a and two surrounding dielectric layers of radii b and c, and permittivities ϵ_1 and ϵ_2, as shown in Figure 4.3. This cylinder is embedded in an infinite region of permittivity ϵ_3. In the experiments that follow, the two dielectric layers are used to model a single insulation layer of a wire enclosed by the substrate layer that supports the electrodes, but in practice wires have multiple insulation layers that could be modeled using this method if the substrate layer contribution can be ignored.
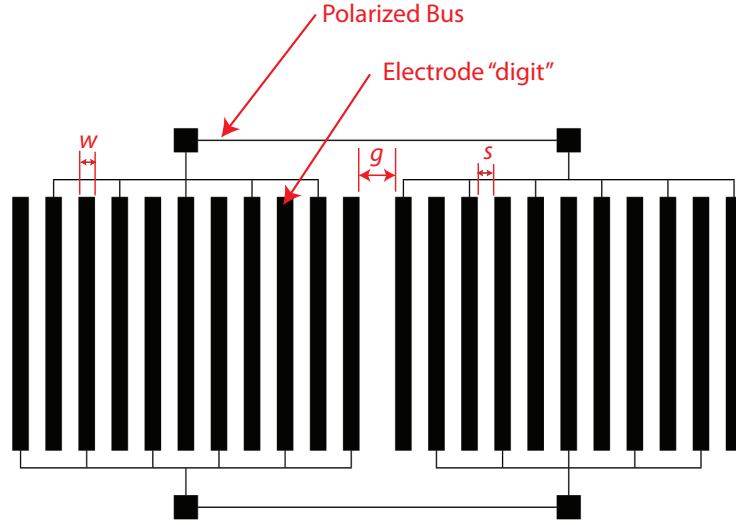
Figure 4.2   Planar schematic of a benchmark cylindrical interdigital sensor with total number of digits $N_{ET} = 22$, $w = s = 1.3$ mm, and $l = 20$ mm. The arc-gap g depends upon the dielectric cylinder radius b to ensure balanced sensor application to the cylinder surface.

4.2.2   Derivation of two-layer cylindrical Green's function

Knowledge of the electrostatic potential Ψ at a point (ρ, ϕ, z) due to a point charge placed at (ρ', ϕ', z') is required to calculate the capacitance of the sensor. The potential is then related to the volume charge density ρ_v by Poisson's equation [2]:

$$\nabla^2 \Psi = -\frac{\rho_v}{\epsilon}, \tag{4.1}$$

where for electrodes on a cylindrical surface, ρ_v will reduce to a surface charge density σ. In order to find a suitable solution to this inhomogeneous partial differential equation, the electrostatic Green's function G at a point (ρ, ϕ, z) due to a point charge placed at (ρ', ϕ', z') must be derived and employed, and is found by solving the following Poisson equation:

$$\left[\frac{1}{\rho} \frac{\partial}{\partial \rho} \left(\rho \frac{\partial}{\partial \rho} \right) + \frac{1}{\rho^2} \frac{\partial^2}{\partial \phi^2} + \frac{\partial^2}{\partial z^2} \right] G(\rho, \phi, z) = -\frac{1}{\rho} \delta(\rho - \rho') \delta(\phi - \phi') \delta(z - z'). \tag{4.2}$$
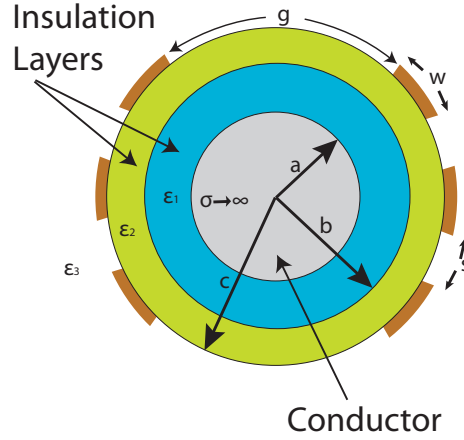
Figure 4.3   Cross-section of the cylindrical interdigital capacitive sensor configuration used in numerical modeling.

The general solution to this equation for both source and observation points exterior to the cylinder is derived in [3] and is of the form:

$$G(\mathbf{r}|\mathbf{r}') = \frac{1}{2\pi^2}\left\{\int_0^\infty \tilde{G}_0(\rho,\rho',\kappa)\cos[\kappa(z-z')]\,d\kappa \right. \tag{4.3}$$

$$\left. +2\sum_{t=1}^\infty \cos[t(\phi-\phi')]\int_0^\infty \tilde{G}_t(\rho,\rho',\kappa)\cos[\kappa(z-z')]\,d\kappa\right\}, \tag{4.4}$$

and for a central conductor that is perfectly conducting and surrounded by two concentric dielectric layers, the Green's function kernel $\tilde{G}_t$ in each region must have the general form:

$$\tilde{G}_t^{(1)}(\rho,\rho',\kappa) = A_t(\kappa)[I_t(\kappa\rho)K_t(\kappa\rho') - \alpha_t(\kappa)K_t(\kappa\rho)K_t(\kappa\rho')], \tag{4.5}$$

$$\tilde{G}_t^{(2)}(\rho,\rho',\kappa) = B_t(\kappa)I_t(\kappa\rho)K_t(\kappa\rho') - \alpha_t(\kappa)C_t(\kappa)K_t(\kappa\rho)K_t(\kappa\rho'), \tag{4.6}$$

$$\tilde{G}_t^{(3)}(\rho,\rho',\kappa) = I_t(\kappa\rho)K_t(\kappa\rho') - \alpha_t(\kappa)D_t(\kappa)K_t(\kappa\rho)K_t(\kappa\rho'), \tag{4.7}$$

where the superscripts (1), (2) and (3) denote regions $a < \rho < b$, $b < \rho < c$ and $\rho > c$, respectively,

$$\alpha_t(\kappa) = \frac{I_t(\kappa a)}{K_t(\kappa a)}, \tag{4.8}$$

and $I_t(\kappa\rho)$ and $K_t(\kappa\rho)$ are the modified Bessel functions of the first and second kind, respectively, of order t. Each of these kernels are composed of two terms that represent incident

and reflected fields due to a point source external to the cylinder, with $C_t(\kappa)$ and $D_t(\kappa)$ acting as reflection coefficients and $A_t(\kappa)$ and $B_t(\kappa)$ acting as transmission coefficients. These four coefficients can be solved by applying four interface conditions:

$$\tilde{G}_t^{(3)}\bigg|_{\rho=c} = \tilde{G}_t^{(2)}\bigg|_{\rho=c} \tag{4.9}$$

$$\epsilon_3 \frac{\partial}{\partial\rho}\tilde{G}_t^{(3)}\bigg|_{\rho=c} = \epsilon_2 \frac{\partial}{\partial\rho}\tilde{G}_t^{(2)}\bigg|_{\rho=c} \tag{4.10}$$

$$\tilde{G}_t^{(2)}\bigg|_{\rho=b} = \tilde{G}_t^{(1)}\bigg|_{\rho=b} \tag{4.11}$$

$$\epsilon_2 \frac{\partial}{\partial\rho}\tilde{G}_t^{(2)}\bigg|_{\rho=b} = \epsilon_1 \frac{\partial}{\partial\rho}\tilde{G}_t^{(1)}\bigg|_{\rho=b}. \tag{4.12}$$

For an arrangement of electrodes on the surface $\rho = c$, the source and observation points exist solely on this surface and are considered to be in region 3. As such, the only coefficient from region 3 that needs to be utilized in Equation (4.3) is $D_t(\kappa)$, which, by solving for the boundary conditions, is given as:

$$D_t(\kappa) = \frac{1}{\alpha_t(\kappa)} \frac{\epsilon_1 I_t'(\kappa c)D_{t1}(\kappa) + \epsilon_2 I_t(\kappa c)D_{t2}(\kappa)}{\epsilon_1 K_t'(\kappa c)D_{t1}(\kappa) + \epsilon_2 K_t(\kappa c)D_{t2}(\kappa)}, \tag{4.13}$$

where

$$\begin{aligned} D_{t1}(\kappa) &= \epsilon_1[I_t(\kappa c)K_t(\kappa b) - I_t(\kappa b)K_t(\kappa c)][I_t'(\kappa b) - \alpha_t(\kappa)K_t'(\kappa b)] \\ &\quad -\epsilon_2[I_t(\kappa c)K_t'(\kappa b) - I_t'(\kappa b)K_t(\kappa c)][I_t(\kappa b) - \alpha_t(\kappa)K_t(\kappa b)], \end{aligned} \tag{4.14}$$

$$\begin{aligned} D_{t2}(\kappa) &= \epsilon_2[I_t'(\kappa c)K_t'(\kappa b) - I_t'(\kappa b)K_t'(\kappa c)][I_t(\kappa b) - \alpha_t(\kappa)K_t(\kappa b)] \\ &\quad -\epsilon_1[I_t'(\kappa c)K_t(\kappa b) - I_t(\kappa b)K_t'(\kappa c)][I_t'(\kappa b) - \alpha_t(\kappa)K_t'(\kappa b)], \end{aligned} \tag{4.15}$$

and $I_t'(\kappa\rho)$ and $K_t'(\kappa\rho)$ are the first derivatives of the modified Bessel functions, expressed as:

$$I_t'(\kappa\rho) = \frac{d}{d\rho}I_t(\kappa\rho) = I_{t+1}(\kappa\rho) - \frac{t}{\kappa\rho}I_t(\kappa\rho) \tag{4.16}$$

and

$$K_t'(\kappa\rho) = \frac{d}{d\rho}K_t(\kappa\rho) = K_{t+1}(\kappa\rho) - \frac{t}{\kappa\rho}K_t(\kappa\rho) \tag{4.17}$$
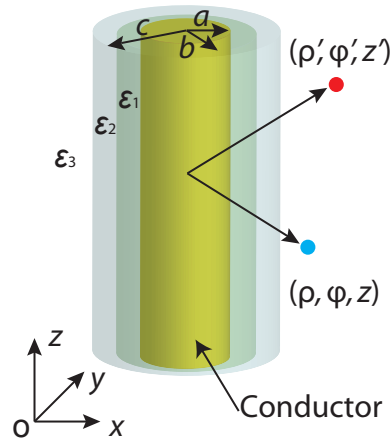
Figure 4.4   Point source exterior to a conducting rod coated with two dielectric layers, assumed infinitely long.

4.3   Numerical implementation

The total capacitance C between the electrodes is calculated in the following sequence. The Green's function for any pair of source and observation points on the outer dielectric surface $\rho = c$ derived in the previous section is used to set up the integral equations relating the Green's function and surface charge density with the potential in the Method of Moments (MoM) calculations. Because of the axisymmetry of the electrode arrangement, only the Green's functions for positive-positive and positive-negative source-observation point pairs, or vice versa, need be calculated. Therefore, the surface charge density requires calculation on either the positive or negative electrodes only. The total capacitance C is then calculated from

$$C = \frac{Q}{V}, \tag{4.18}$$

where the total charge Q on either the positive or negative electrodes is obtained by integrating the surface charge density over each electrode surface and V is the potential difference, or voltage, between the electrodes.
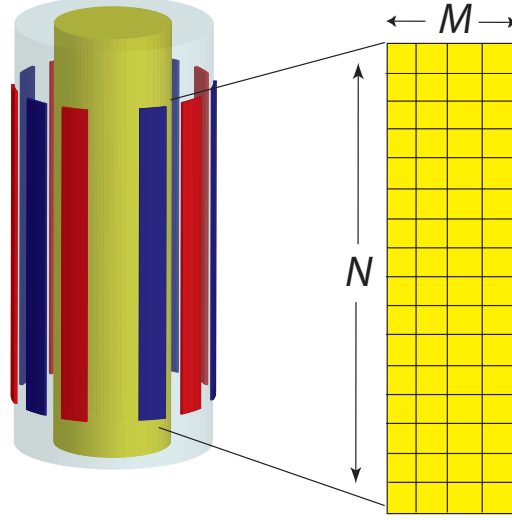
Figure 4.5   Discretization of the surface of a single digit into M elements in the ϕ-direction and N elements in the z-direction, each with assumed constant surface charge density.

4.3.1   Calculation method

Figure 4.5 shows the discretization of a single digit surface into $M \times N$ elements, each with an assumed constant surface charge density. Each digit is discretized into M elements in the ϕ-direction and N elements in the z-direction. The surface charge density on the Side 1 digits is denoted as $\sigma_n(\phi', z')$ and that on the Side 2 digits as $\sigma_n(\phi' + \pi, z')$, where n is the digit number. The potential Ψ at the observation point $\mathbf{r} = (c, \phi, z)$ on the electrode surface can be expressed by integrating (4.3) over the individual digit surfaces:

$$
\begin{aligned}
\Psi(\phi, z) \quad &= \frac{c}{\epsilon_0} \sum_{n=1}^{2N_E+1} \left\{ (-1)^{n+1} \iint_{\text{Side 1}} G^{(1)}(\mathbf{r}|\mathbf{r}') \sigma_n(\phi', z')\, d\phi'\, dz' \right. \\
&\left. + (-1)^n \iint_{\text{Side 2}} G^{(1)}(\mathbf{r}|\mathbf{r}') \sigma_n(\phi' + \pi, z')\, d\phi'\, dz' \right\}.
\end{aligned}
\tag{4.19}
$$

In the MoM calculations, the following expansion is used to approximate the continuous function $\sigma_n(\phi', z')$:

$$
\sigma_n(\phi', z') = \sum_{j=1}^{MN} \sigma_j b_j(\phi', z'),
\tag{4.20}
$$

where σ_j is the unknown constant surface charge density on element j and $b_j(\phi', z')$ is the pulse basis function

$$
b_j(\phi', z') = \begin{cases} 1 & \text{on element } j \\ 0 & \text{elsewhere.} \end{cases}
\tag{4.21}
$$

To solve for the MN unknown coefficients σ_j, weighting functions $w_i(\phi, z)$ are introduced to force the boundary condition for the potential in (4.19) to be satisfied for each element on the sensor surface. The point-matching method is utilized, in which the weighting functions are Dirac delta functions:

$$w_i(\phi, z) = \delta(\phi - \phi_i)\delta(z - z_i) \quad \text{on element } i, \tag{4.22}$$

where $i = 1, 2, ..., L$ where $L = MN$. Discretizing the integral equation using weighting functions in each of the L elements, (4.19) is expressed as the following matrix equation:

$$
\begin{pmatrix}
G_{11} & G_{12} & \dots & G_{1L} \\
G_{21} & G_{22} & \dots & G_{2L} \\
\vdots & \vdots & \ddots & \vdots \\
G_{L1} & G_{L2} & \dots & G_{LL}
\end{pmatrix}
\times
\begin{pmatrix}
\sigma_1 \\
\sigma_2 \\
\vdots \\
\sigma_L
\end{pmatrix}
=
\begin{pmatrix}
\Psi \\
\Psi \\
\vdots \\
-\Psi
\end{pmatrix},
\tag{4.23}
$$

where

$$G_{ij} = \frac{c}{\epsilon_0} \iint_{\text{element } j} G^{(1)}(\mathbf{r}_i|\mathbf{r}'_j)b_j(\phi', z')d\phi'dz'. \tag{4.24}$$

If a uniform mesh, whereby the dimensions of each element are the same, is used in the MoM calculations, then (4.24) can be simplified as

$$
\begin{aligned}
G_{ij} \quad &= \frac{c}{2\pi^2\epsilon_0} \left\{ \Delta\phi \int_0^\infty \tilde{G}_0^{(1)}(\kappa) \cos[\kappa(z_j - z_i)]\frac{2}{\kappa} \sin\left(\frac{\kappa\Delta z}{2}\right) d\kappa \right. \\
&\quad + 2\sum_{t=1}^\infty \cos[t(\phi_j - \phi_i)]\frac{2}{t} \sin\left(\frac{t\Delta\phi}{2}\right) \\
&\quad \left. \times \int_0^\infty \tilde{G}_t^{(1)}(\kappa) \cos[\kappa(z_j - z_i)]\frac{2}{\kappa} \sin\left(\frac{\kappa\Delta z}{2}\right) d\kappa \right\},
\end{aligned}
\tag{4.25}
$$

where $\Delta\phi$ and Δz are the width and length of each element in the ϕ- and z-directions, respectively, and (ϕ_i, z_i) and (ϕ_j, z_j) are the center coordinates of the source and observation elements, respectively. From (4.24) the surface charge density $\sigma_n(\phi', z')$ on one of the polarized electrode arrays is solved, and that for the other electrode is simply $-\sigma_n(\phi' + \pi, z')$. The total charge Q on each polarized electrode array can be found by integrating $\sigma_n(\phi', z')$ over the electrode array surface. The sensor output capacitance C is finally calculated through (4.18).

4.3.2   Example calculations

When numerically evaluating the Green's function matrix element in (4.25), the infinite integrals and summation require finite truncation. Although the convergence of the integrands depends on the cylinder and electrode geometry and dielectric layer contrasts, a typical arrangement of electrodes is analyzed here to determine behavior of the integrands and truncation limits to achieve three significant figures of accuracy in the calculated capacitance output, which is sufficient for comparison with the experimental data.

According to the formulation given in Section 4.3.1, the minimum total number of electrodes N_{ET} is 6, and for a cylinder of real aircraft wire proportions, $w = 0.1$ mm, $s = 0.6$ mm, and $l = 25.4$ mm. This cylinder has dimensions $a = 0.4953$ mm, $b = 1.0795$ mm, and a substrate layer radius of $c = 1.1049$ mm. The cylinder and the substrate have relative permittivity values of $\epsilon_{r1} = 4.015$ and $\epsilon_{r2} = 2.84$, respectively. The relative permittivity for the cylinder was calculated as an average, or effective, permittivity, which is a function of the individual layer thicknesses in Table 3.1 and the permittivity values for those layers at 1 MHz, given in [4]. For all experiments described in this chapter, the number of elements in a direction per electrode is $M = N = 10$. For the diagonal matrix components, where the source and observation elements are collocated, the cosine terms in Equation (4.25) become unity, eliminating much of the oscillatory behavior of the integrand and causing the integrand to converge to zero at a much slower rate. Because of this, and to guarantee a well-conditioned matrix upon inversion, the diagonal terms in the numerical evaluation require higher finite truncation values than the off-diagonal terms (in these calculations, a factor of three is used).

Figure 4.6 shows the convergence behavior of the capacitance for the above described electrode configuration as a function of the integral and summation truncation limits. From the figure, it is observed that, for a given summation truncation number, the capacitance oscillates and converges to a constant value as the integration limit increases, and for a given integration limit, the capacitance decreases toward a constant value as the summation truncation number increases. For a summation truncation number of 50 and integration limit of 6000, the output capacitance has a reliable precision of 3 significant figures, which is also the apparent limit of
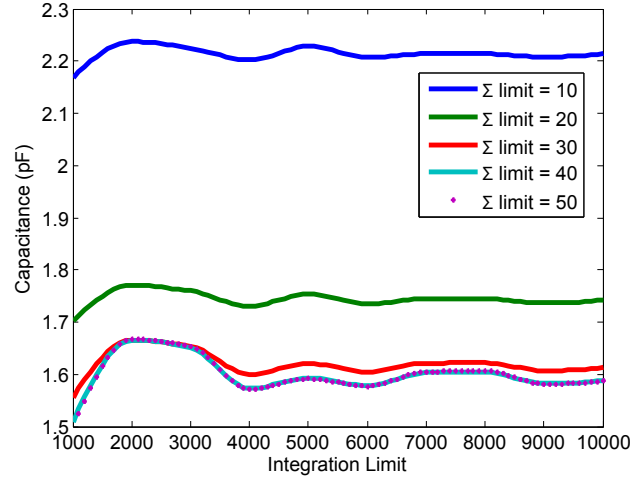
Figure 4.6   Example of converging output capacitance as a function of integration limit and number of terms in the summation(Σ) used in calculating the Green's function of Equation (4.25). In this particular case, $a = 0.4953$ mm, $b = 1.0795$ mm, and $c = 1.1049$ mm. The cylinder and the substrate have relative permittivity values of $\epsilon_{r1} = 4.015$ and $\epsilon_{r2} = 2.84$, respectively.

the measurement device accuracy described in Section 4.5. Therefore, 50 summation terms and an integration limit of 6000 will be used in all calculations hereafter given in this chapter.

The dependence of the sensor capacitance on the various electrode configuration parameters is investigated as follows. In Figure 4.7, the output capacitance is plotted as a function of the insulation relative permittivity ϵ_{r1} where different electrode configurations are considered. The wire is again modeled as a cylinder with $a = 0.4953$ mm, $b = 1.0795$ mm and $c = 1.1049$ mm with a substrate relative permittivity value of $\epsilon_{r2} = 2.84$. The default electrode configuration is $w = s = 0.1$ mm, $l = 25.4$ mm and $N_{ET} = 6$. For any of the electrode configurations given in the figure, a linear relationship between the capacitance and the permittivity is clearly observed. This slope, $\Delta C/\Delta\epsilon$, can be viewed as the sensitivity of the capacitive sensor to changes in the insulation permittivity and is given for each configuration in Table 4.1. It should be noted that this definition of sensitivity has units of meters, which is related to the ratio of the area of the electrodes to the distance between them. Increasing the length l of the electrodes by a factor of 2 doubles the output capacitance and the sensitivity due to the doubling of the total charge. Increasing the electrode spacing s by a factor of 2 decreases the output capacitance as would be
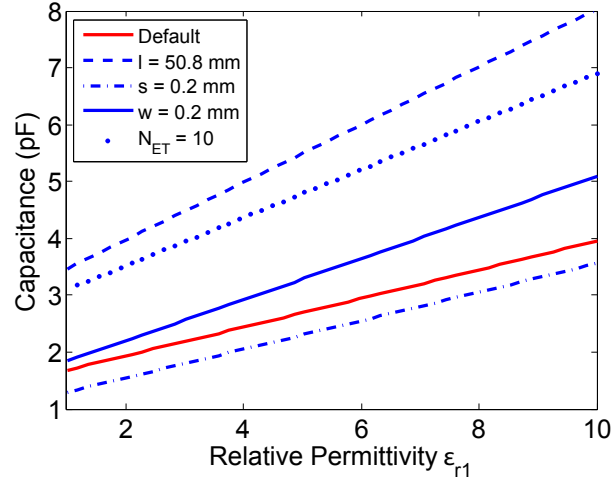
Figure 4.7   Calculated sensor capacitance as a function of insulation permittivity. The default sensor configuration is $w = s = 0.1$ mm, $l = 25.4$ mm, and $N_{ET} = 6$ unless otherwise indicated in the legend.

Table 4.1   Sensitivity values of the electrode configurations given in Figure 4.7. The default sensor configuration is $w = s = 0.1$ mm, $l = 25.4$ mm, and $N_{ET} = 6$ unless otherwise indicated in the "Parameter" column.

Parameter	$\Delta C/\Delta\epsilon_1$ (mm)
Default	28.49
$l = 50.8$ mm	57.32
$s = 0.2$ mm	28.40
$w = 0.2$ mm	40.82
$N_{ET} = 10$	47.79

expected, but the sensitivity decreases only slightly, due to the effect of the penetration depth that will be discussed in Section 4.4. Increasing the electrode width w by a factor of 2 also doubles the total area of the electrodes allowing more charge to be stored, but the dimensions of the interelectrode region remain the same and so the capacitance increases only slightly but with higher sensitivity. Adding four more electrodes increases the total electrode area and sensing area between the electrodes, which increases the total capacitance and sensitivity.

4.4   Field penetration optimization

The cylindrical interdigital sensor described in this chapter has, up to this point, been designed primarily for i) the smallest achievable measurement error of 0.1% in the LCR meter measurements and ii) for greatest sensitivity to changes in permittivity of the entire insulation layer. Here we consider another factor in the sensor design: the depth of penetration of the electric field into the insulation layer. Penetration depth is commonly referred to as skin depth in the interaction of a dynamic electric field with a lossy material, such as a real conductor, and is defined as the distance into the conductor at which the magnitude of a transmitted electromagnetic wave falls to $1/e$ (about 37%) of its value at the material boundary. In an electrostatic or electroquasistatic interaction with a low-loss dielectric, however, penetration depth must be defined differently.

4.4.1   Calculation method

Penetration depth is an important sensor characteristic when localized flaws could occur at various depths or layers within the insulation of a wire. Also, because the electric field generated by the interdigital sensor fringes between oppositely-charged electrodes and couples perpendicularly to the central conductor, it is the goal to design the most efficient sensor that balances both of these effects. Prior work in [5] defines the penetration depth for a coplanar capacitive sensor (designed for characterizing flat, laminar dielectrics) as the thickness of the dielectric material for which the measured capacitance has experienced a 10% change from the constant value C_0 measured on a half-space of the same material. In this case of a test-piece with cylindrical geometry and central conductor, a similar definition of penetration depth δ can be made as

$$\delta = b - a_{10} \tag{4.26}$$

where, referring to Figure 4.1, a_{10} is the radius of the central conductor for which the capacitance of the sensor has increased by 10% compared with that for $a = 0$, i.e. for the case in which there is no central conductor. Essentially, δ represents the theoretical thickness of the wire insulation by which the capacitance has increased by 10% from that for $a = 0$.
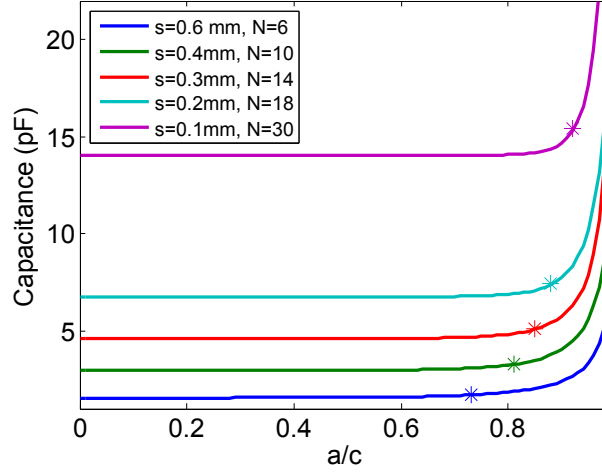
Figure 4.8   Calculated C for sensors with several different total digits and electrode spacing as a function of conductor radius a. In this case, $b = 1.0795$ mm, $c = 1.1049$ mm, $\epsilon_{r1} = 4.015$, $\epsilon_{r2} = 2.84$, and $w = 0.1$ mm. The * on each plot indicates the point where the capacitance has increased by 10% from C_0.

To determine the effective penetration depth of an actual wire sensor, numerical simulations were conducted on the theoretical wire described in Section 4.3.2 in which the radius of the central conductor was varied from 0 to c while holding all other parameters constant. Because the penetration depth of the interdigital configuration depends on the separation between the electrodes, calculations were also conducted for five different values of s and N_{ET}. The results of this simulation are shown in Figure 4.8.

Considering the data plotted in Figure 4.8 it can be seen that, as a vanishes, the total capacitance approaches a constant value C_0, which is to be expected since the electric field no longer couples with the central conductor, leaving only the fringing field between neighboring digits. This effect is illustrated in Figure 4.9(a), where the insulation thickness t is much greater than the digit spacing s so that the field generated between the digits held at potentials of $V+$ and $V-$ dominates any coupling with the central conductor held at a potential of 0 V. When $a \to c$, the capacitance tends toward infinity, which is characteristic of the inverse distance relationship in a parallel plate capacitor, the field of which is illustrated in Figure 4.9(b). In essence, a_{10} represents one point of balance between the fringing and parallel fields, illustrated in Figure 4.9(c), and an most efficient sensor may be expected to have $\delta = t = b - a$, where t is

(a) Fringing field dominance when $t \gg s$

(b) Parallel field dominance when $t \ll s$

(c) Balanced field for optimal penetration depth
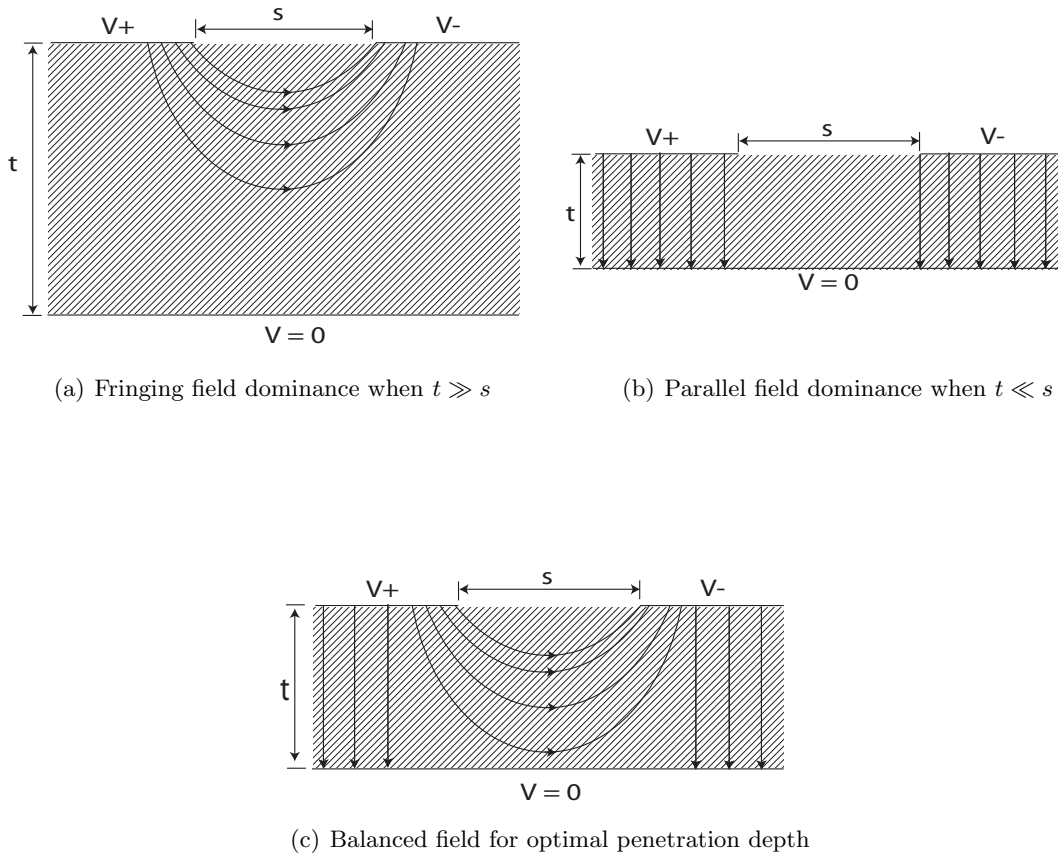
Figure 4.9   Schematic diagram showing the electric field coupling to a ground plane (here representing the wire's the central conductor at potential $V = 0$) as a function of digit spacing s and insulation thickness t.

the thickness of the wire insulation. The data from Figure 4.8 are provided in detail in Table 4.2.

It is observed from this data that $a_{10} \to c$ as the spacing between the digits decreases, meaning that the penetration depth also decreases. This is to be expected since a decreasing electrode spacing will result in a greater concentration of the projected electric field nearer to the surface coplanar with the electrodes. From Table 4.2 it can be seen from the penetration efficiency δ/t that the most efficient sensor at penetrating the wire insulation is the one with the greatest electrode spacing, however, at a significantly reduced output capacitance. Conversely, the sensor with the greatest output capacitance will have the lowest penetration efficiency. Ultimately, the chosen sensor design should be a balance between maximum capacitance and

Table 4.2   Results of the penetration depth simulation in Figure 4.8.

	$N_{ET} =$	6	10	14	18	30
C_0	(pF)	1.56	2.99	4.63	6.76	14.0
C_{10}	(pF)	1.72	3.29	5.10	7.44	15.4
a_{10}/c		0.73	0.81	0.85	0.88	0.94
a_{10}	(mm)	0.81	0.89	0.94	0.97	1.0
δ	(mm)	0.27	0.18	0.14	0.11	0.06
δ/t	(%)	47	32	24	18	11

penetration efficiency, which in this case would be any number of digits between 6, the minimum, and 30, the maximum considering manufacturing tolerances and the wire dimensions.

4.5   Experimental verification

4.5.1   Benchmark experiments

Benchmark capacitive experiments were carried out for the purpose of validating the modeled results in certain cases. Four sets of planar interdigital electrodes, examples of which are shown in Figures 4.10 and 4.2, were fabricated using photolithographic techniques by American Standard Circuits, Inc. The electrodes were etched from a 17.8 μm thick bare copper cladding deposited on a 100 μm thick Kapton® polyimide film substrate to form a flat flexible sensor. These sensors were then conformably fixed to the outer dielectric surface of three different dielectric-coated conductive cylinders to form the cylindrical interdigital capacitive sensors. Two sets of the sensors had differing electrode widths, $w = s = 0.9$ mm and 1.3 mm, with each set having two electrode lengths, $l = 20$ mm and 40 mm. Based on the circumferences of the dielectric-coated conductive cylinders and to maximize the number of digits, the sensors with $s = w = 0.9$ mm are comprised of 30 total digits and those with $s = w = 1.3$ mm are comprised of 22 total digits. These electrode configurations were designed to produce capacitance values that, at 1 MHz, resulted in the best LCR meter instrument accuracy, lying in the approximate range 0.1 to 0.3% [1].

Three 152.4-mm-long dielectric-coated conductive cylinders are used in the measurements
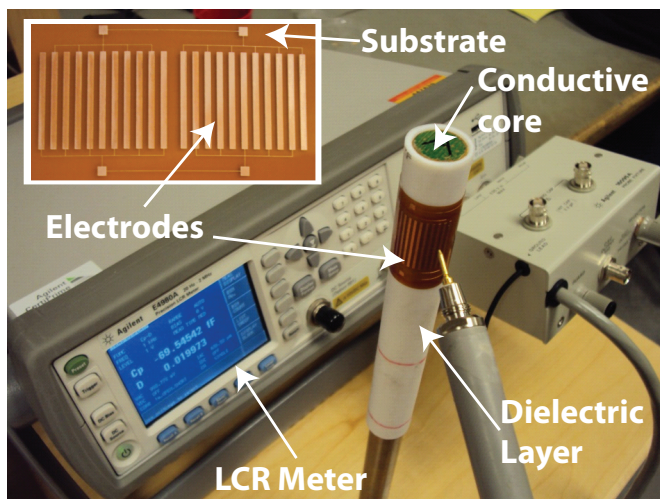
Figure 4.10   Agilent E4980A precision LCR meter and Agilent probe test fixture 16095A used for sensor capacitance measurements. Subfigure: photograph of the flexible rectangular planar electrodes fabricated using photolithography.

to simulate an infinitely long cylindrical dielectric rod. These cylinders were significantly longer than the electrode lengths in order to legitimately neglect the edge effects during a measurement. The three different dielectric materials were Tecaform™ acetal copolymer, cast acrylic, and Teflon® polytetrafluoroethylene (PTFE). The permittivity of each dielectric was measured independently using a Novocontrol Alpha Dielectric Spectrometer at 1 MHz. The parameters of these cylinders are listed in Table 4.3. It also merits mention that in order to maintain exact electrode widths and spacings for cylinders of slightly varying radii, the arc-gaps g for the 22-digit sensors were set to 3.3 mm, 3.1 mm, and 3.3 mm for Tecaform™, acrylic, and Teflon® dielectric coatings, respectively. For the 30-digit sensors g was set to 4.5 mm, 4.3 mm, and 4.5 mm for the same respective materials.

The planar interdigital electrodes were then conformally wrapped around the surface of the dielectric cylinder with the bare copper facing outward to allow for easy contact with the LCR meter, introducing the additional Kapton® substrate layer of radius c. The edges of the Kapton® substrate were then tightly taped to each other to eliminate any air gap between the dielectric and substrate layers as much as possible.

The sensor output capacitance was measured using an Agilent E4980A Precision LCR meter

Table 4.3 Parameters of the dielectric-coated conductive cylinders used in benchmark experiments. The permittivity was measured independently on disc-shaped polymer samples, using a Novocontrol Alpha Dielectric Spectrometer [12].

Dielectric material	Conductor radius a (mm)	Dielectric radius b (mm)	Cylinder length (mm)	Measured permittivity at 1 MHz
Tecaform$^{\text{TM}}$	7.95 ±0.005	9.64 ±0.015	152.4	3.77 ±0.05
Acrylic	7.95 ±0.005	9.59 ±0.02	152.4	3.02 ±0.05
Teflon$^{®}$	7.95 ±0.005	9.66 ±0.01	152.4	2.21 ±0.04

operating at 1 MHz. This frequency had a twofold benefit, the first being that the error listed in the operating manual for a 10 pF measurement was approximately 0.1%, the minimum possible. Secondly, the wavelength in free space, 300 m, is much greater than the length of the electrodes, meaning that there are no nodes, standing waves, reflections, or phase delays between the electrodes. Thus the quasistatic regime assumed in the numerical model is valid.

After calibration, each capacitance measurement was made by placing the LCR meter probe points in contact with a pair of adjacent sensor digits. The LCR meter was set to display an average of 16 measurements which were manually recorded. Although 7 significant figures were displayed and recorded, only 3 were determined to be consistent and, therefore, accurate. Measured values for each of the four sensor configurations are compared with the numerically calculated values in Figs. 4.11 and 4.12. The mean agreement between the calculated and measured values is 5%.
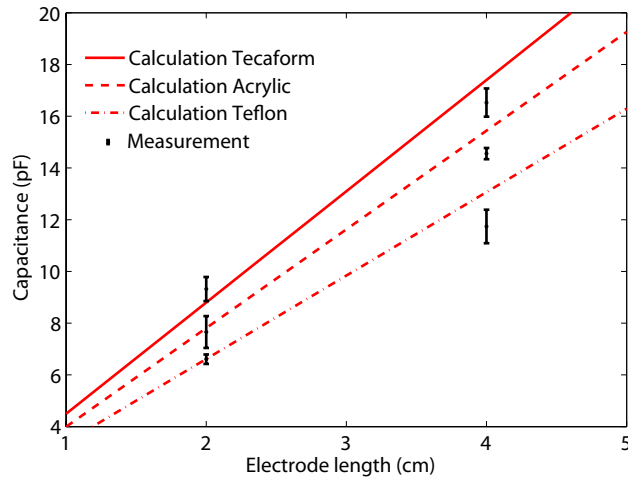
Figure 4.11   Measured and calculated C for a 22-digit sensor as a function of electrode length l. The plotted measurement values are an average of five measurements and the error bar denotes ± 1 standard deviation of these measurements.
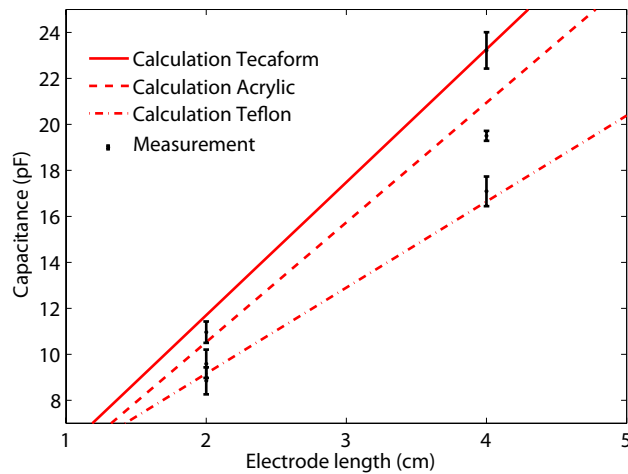

Figure 4.12   Measured and calculated C for a 30-digit sensor as a function of electrode length l. The plotted measurement values are an average of five measurements and the error bar denotes ± 1 standard deviation of these measurements.

4.6   Conclusion

A quasielectrostatic numerical model, based on the Green's function due to a point source exterior to an infinitely long cylindrical conductive cylinder coated with two different dielectric materials, has been developed to quantitatively evaluate the permittivity of cylindrical test-pieces. This model has been validated by large-scale benchmark capacitive measurements which show agreement with the model to within 5%. Clamps with integrated interdigital sensors are currently being developed that will be used to nondestructively evaluate wire insulation in critical structures, primarily aircraft. The electrodes designed for these clamp fixtures have undergone an optimization of the electric field penetration depth to make the sensor more accurate and efficient at measuring degradation levels in wire insulation.

4.7   References

[1] *Agilent E4980A Precision LCR Meter: User's Guide*, 8th Edition, Agilent Technologies, 2010.

[2] M. N. O. Sadiku, *Numerical Techniques in Electromagnetics with MATLAB®*. 3rd Edition. Boca Raton: CRC Press, 2009.

[3] T. Chen and N. Bowler, "Analysis of a capacitve sensor for the evaluation of circular cylinders with a conductive core", *Meas. Sci. Technol.*, Vol. 23, 045102(10pp), 2012.

[4] G. L. Johnson, *Solid State Tesla Coils*. Manhattan: Kansas State University, 2001.

[5] T. Chen and N. Bowler, "A Rotationally Invariant Capacitive Probe for Materials Evaluation", *Materials Evaluation*, Vol. 70, No. 2, pp. 161-172, 2012.

CHAPTER 5. GENERAL CONCLUSION

5.1 Discussion

The research presented in this thesis is motivated by the need within the aerospace industry to characterize wire insulation for the purpose of detecting poor insulators that may result in dangerous situations in-flight. Extant resistive and capacitive characterization methods are explored to determine the effectiveness and quality of the results in the measurement of their respective parameters of resistance and capacitance. To better understand the electric field distribution within and external to an insulated wire generated by capacitive electrodes, a simplified analytical model was developed in Chapter 2 that includes a variable central conductor potential. It was determined that this charged conductor will have no effect on the capacitance because it depends only on the geometry and material properties of a symmetrical electrode configuration. In Chapter 3, a description is given of resistance measurements taken with a commercial insulation tester to determine the effect of degradation on the conductivity of the insulation of 17 retired aircraft wire samples. The results showed significantly reduced resistance measurements for wires that were qualitatively observed to be significantly degraded. Timed resistance tests also showed that the insulation of these same wires fell into the category of being "questionable", as defined by the instrument test procedures, with DAR values between 1.0 and 1.2, as opposed to wires classified as "good" with DAR values between 1.4 and 1.6. Curved patch-electrode capacitive sensors were also applied, as described in Chapter 3, to the same 17 wire samples. The measured dissipation factor, defined as the ratio of the imaginary to the real parts of the measured capacitance, in these experiments was found to be significantly higher for the degraded samples than for the non-degraded samples and showed a good pattern of agreement with the results of the resistance tests. A novel cylindrical

interdigital capacitive sensor was developed and tested in Chapter 4, the motivation behind which was to increase the signal-to-noise ratio, reduce the measurement error, and increase the circumferential coverage of the sensor around a wire. Benchmark experiments performed on large-scale dielectric-coated conductive cylinders delivered results that agreed to within 5% of those generated by the numerical model also described in Chapter 4. A method for analyzing the electric field penetration depth within the insulation was also developed. This was achieved by varying the radius of the central conductor in the numerical model until it was "sensed" by the interdigital electrodes.

5.2   Recommendations for future research

Interdigital capacitive sensors designed using the penetration depth optimization technique are currently being developed for onboard aircraft testing an, ultimately, for use by aircraft maintenance personnel. These sensors are to be affixed to hand-held clamps, shown in Figure 5.1, the jaws of which utilize the milled arc design of the patch-electrodes in Chapter 3 to securely grasp the wire. These new interdigital clamp sensors will be tested on the same 17 wire samples described in Chapters 2 and 3 to assess the designed improvements in the interdigital design.

For future experiments, it is also worth exploring the results achieved by sweeping through a range of frequencies in the capacitive measurements instead of a single frequency. It is known from research by Debye and many others that dielectric relaxations occur at specific
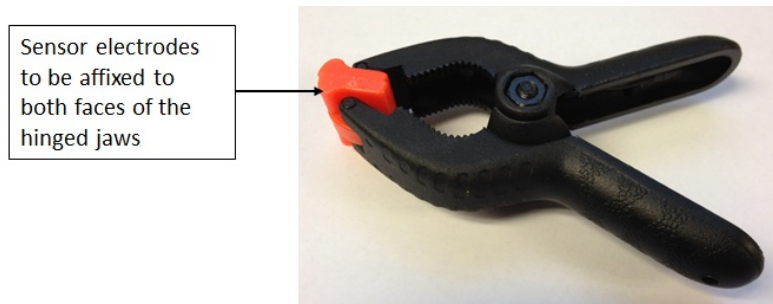

Figure 5.1   Plastic spring-loaded clamp with two orange jaws that will be used to support and apply the interdigital electrodes to both sides of an aircraft wire.

frequencies for specific polymers. Experiments in [1] show that thermal exposure causes changes in the measured permittivity at different frequencies. This spectral analysis of wire insulation could yield valuable new information and improve sensitivity in the detailed characterization of specific types of wiring insulation in critical structures.

5.3   References

[1] L. Li, N. Bowler and M. R. Kessler, "Dielectric Response of PTFE and ETFE Wiring Insulation to Thermal Exposure", *IEEE Trans. Dielectr. Electr. Insul.*, Vol. 17. No. 4, pp. 1234-1241, 2010.

ACKNOWLEDGEMENTS

I would like to express my deep and sincere gratitude to my major professor, Dr. Nicola Bowler. Her guidance, encouragement, and attention to detail over these past few years have taught me invaluable lessons that have made me a better student, researcher, and engineer. I am honored to have completed my master's degree under her tutelage and I look forward to continuing with her as my Ph.D. advisor.

I would like to thank Dr. Jiming Song for his highly valuable knowledge of electromagnetics and for always leaving his door open when I had homework, research, and programming questions. The majority of my coursework has been classes taught by Dr. Song and I have learned a lot from him. I would also like to especially thank Dr. Tianming Chen for invaluable and innumerable conversations that have greatly contributed to my knowledge and understanding of electromagnetics. I would not be at this point in my academic career if it were not for him. Dr. Hui Xie and Dr. Yang Li also deserve recognition for their contributions to my understanding of analytical and computational electromagnetics and for their efforts to better my research.

Finally, I would like to my parents, Kevin and Vicki, and my sister, Laura, for their endless love and support throughout these past few years and beyond. They have always supported the decisions I have made in my career and words cannot express the comfort that has given me.